VOL 01, N° 09

ISSN 2952-8291

Belgian Journal of Physics

The official magazine of the Belgian Physical Society

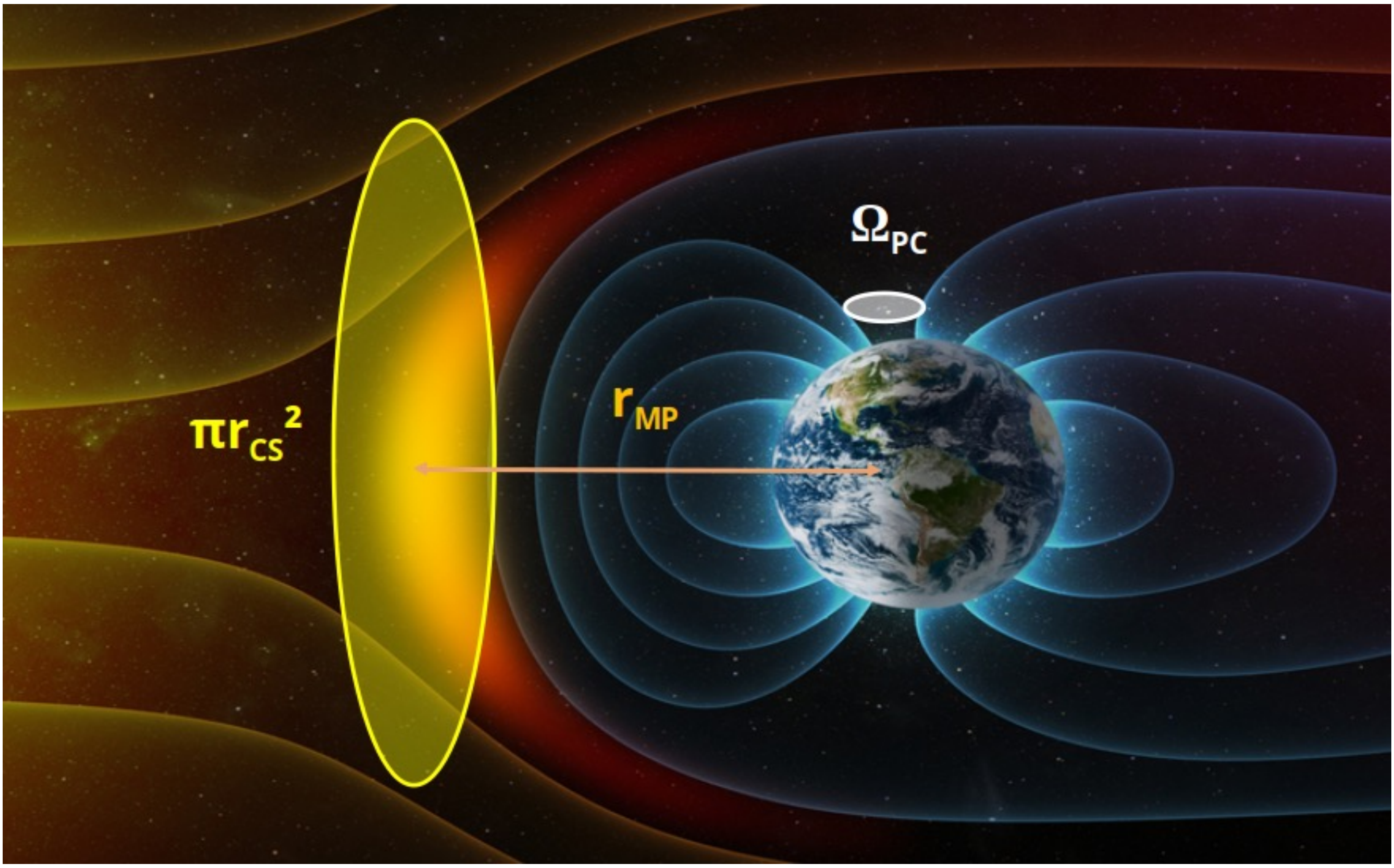

Belgian Physical Society

www.belgianphysicalsociety.be

Belgian Journal of Physics

Belgische Natuurkunde Vereniging/Société Belge de Physique Belgische Physikalische Gesellschaft/Belgian Physical Society

v.z.w./a.s.b.l./V.o.G

VOL 01, N° 09

ISSN 2952-8291

Belgian Journal of Physics

The official magazine of the Belgian Physical Society

Dear Readers,

This year's Nobel Prize in Physics celebrates a feat that sounds like science fiction: *macroscopic quantum tunnelling and energy quantisation in an electric circuit.* The prize was awarded jointly to **John Clarke**, **Michel H. Devoret**, and **John M. Martinis** "for the discovery of macroscopic quantum-mechanical tunnelling and energy quantisation in an electric circuit".

Quantum mechanics has always carried a whiff of the mystical. Electrons can tunnel through barriers they shouldn't cross; atoms can be in two places at once. But until a few decades ago, such behaviour seemed confined to the microscopic realm. Larger systems, messy and noisy, were thought to lose their "quantumness" through decoherence. Then came the superconducting circuit. By cooling metal loops to a few mK and designing them with exquisite care, Clarke, Devoret, and Martinis demonstrated that an entire macroscopic electric circuit could behave quantum-mechanically—exhibiting quantised energy levels and tunnelling phenomena

One of the phenomena honoured this year is **macroscopic quantum tunnelling**. In essence, a current trapped in a potential well can "leak" through an energy barrier without climbing over it—thanks to quantum mechanics. The twist: the "particle" doing the tunnelling isn't a single electron but the collective state of many electrons in the superconducting circuit. Imagine a whole marching band ghosting through a wall in perfect formation. That this can happen in a device you can hold in your hand is remarkable. Such experiments form the technological underpinnings of superconducting qubits, Josephson junctions, and SQUIDs.

For decades physicists asked: where does quantum behaviour give way to classical reality? These experiments show that the divide is more illusion than boundary. Under the right conditions—near absolute zero, perfect isolation, and clever engineering—even macroscopic systems can obey the Schrödinger equation. The implication is profound: the classical world isn't a different realm; it's just what quantum mechanics looks like when blurred by noise and measurement.

A century ago, Schrödinger's cat was a metaphor. Today, it's hardware. The same principles that puzzled philosophers now power real superconducting qubits and quantum technologies. The 2025 Nobel honours more than a clever experiment—it honours a paradigm shift: physics stepping off the chalkboard and into the fabrication lab. Clarke, Devoret, and Martinis didn't just prove a point; they enabled a new age of quantum engineering.

One hundred years after quantum mechanics emerged, the boundary between the microscopic and the macroscopic is dissolving. The 2025 Nobel Prize in Physics reminds us: the quantum world isn't elsewhere—it's right here, humming quietly in a superconducting loop in a fridge at a few mK.

Fabrice Louche
Editor in Chief

Leveraging modular values in quantum algorithms: the Deutsch-Jozsa algorithm

Lorena Ballesteros Ferraz [1,2,3], **Timoteo Carletti** [2,4], **and Yves Caudano** [1,2,3]

[1] naXys, Namur Institute for Complex Systems, University of Namur, Belgium
[2] NISM, Namur Institute of Structured Matter, University of Namur, Belgium
[3] Research Unit Lasers and Spectroscopies (UR-LLS), Department of Physics, University of Namur, Belgium
[4] Department of Mathematics, University of Namur, Belgium

We present a novel approach to quantum algorithms, by taking advantage of modular values, i.e., complex and unbounded quantities resulting from specific post-selected measurement scenarios. Our focus is on the problem of ascertaining whether a given function acting on a set of binary values is constant (uniformly yielding outputs of either all 0 or all 1), or balanced (a situation wherein half of the outputs are 0 and the other half are 1). Such problem can be solved by relying on the Deutsch-Jozsa algorithm. The proposed method, relying on the use of modular values, provides a high number of degrees of freedom for optimizing the new algorithm inspired from the Deutsch-Jozsa one. In particular, we explore meticulously the choices of the pre- and post-selected states. We eventually test the novel theoretical algorithm on a quantum computing platform. While the outcomes are currently not on par with the conventional approach, they nevertheless shed light on potential for future improvements, especially with less-optimized algorithms. We are thus confidend that the proposed proof of concept could prove its validity in bridging quantum algorithms and modular values research fields.

Introduction

Numerous quantum algorithms have demonstrated theoretically superior efficiency compared to their presently known classical counterparts, with historical examples including database search [1] and integer factorization [2]. Among the earliest instances of this superiority are the Deutsch algorithm [3] and its generalization, the Deutsch-Jozsa algorithm [4]. The Deutsh-Jozsa algorithm addresses the verification of whether a binary function acting on n classical bits, $f : \{0,1\}^n \to \{0,1\}$, is balanced or constant. The function is constant if it has the same output for all possible values of the n input bits, while it is balanced if it is equal to 0 for exactly half of the possible values of the input bits (and 1 for the other half). Remarkably, the quantum approach accomplishes this task in a single step, while the best classical algorithm necessitates $2^n - 1$ repetitions in the worst-case scenario.

A weak value $A_w = \frac{\langle \psi_f | \hat{A} | \psi_i \rangle}{\langle \psi_f | \psi_i \rangle}$ is an unbounded complex number involving a Hermitian operator $\hat{A}$, as well as an initial state $|\psi_i\rangle$ and a final state $|\psi_f\rangle$, respectively called pre- and post-selected states in this context. The concept of weak values of observables arises from a quantum process, called weak measurement, that involves pre- and post-selection, as introduced in the work of Aharonov, Albert, and Vaidman (AAV) in the 1980s [5]. In this protocol, the whole quantum system is composed of an ancillary component acting as a measuring device and a primary system of interest. At the outset, this combined entity is described by the separable quantum state $|\Psi\rangle = |\psi_i\rangle \otimes |\phi\rangle$, where the pre-selected state $|\psi_i\rangle$ is the state in which the system of interest is set prior to the measurement, while $|\phi\rangle$ represents the initial state of the ancillary component. The protocol unfolds in four steps. Initially, the system's pre-selection occurs, involving the selection of the initial state $|\psi_i\rangle$ of the system of interest and the preparation of the ancillary state $|\phi\rangle$. Subsequently, an interaction occurs between the system and the ancillary component, which is mathematically modeled by the Hamiltonian operator $\hat{H} = \hbar\, g(t)\, \hat{A} \otimes \hat{p}$ inspired from the von Neumann protocol for quantum measurement. Here, the coupling parameter $g(t)$ determines the interaction coupling strength, which typically emerges as a small factor in the process, approximately given by $\gamma = \int_{t_i}^{t_f} g(t)\, dt \ll 1$ [5], where $t_f - t_i$ is the short interaction duration. The operator $\hat{p}$ represents the momentum operator of the measuring device. The observable $\hat{A}$ corresponds to the physical quantity probed by the protocol. The (weak) interaction entangles (slightly) the system of interest and the ancillary component. Finally, a post-selection stage follows: it involves a projective measurement and filtering applied to the system, throwing away cases in which the system of interest does not end up in the desired final state $|\psi_f\rangle$. Conditioned on a successful post-selection of $|\psi_f\rangle$, a measurement of the ancillary component is performed to extract information about the weak value, obtained from the shift of the average of a meter observable. Typically, the ancilla's wavefunction in position representation is shifted by the real part of the weak value, while the ancilla's wavefunction in momentum representation is shifted by the imaginary part of the weak value. The modular value, expressed as

$$A_m = \frac{\langle \psi_f |\, e^{-ik\hat{A}}\, |\psi_i\rangle}{\langle \psi_f | \psi_i \rangle}, \tag{1}$$

arises from a protocol similar to the one of weak measurements, in which pre- and post-selection is necessary. However, modular values are unique as they are associated with interactions of any strength because they involve a qubit as the ancillary meter component [6], rendering a weak coupling between the system and ancilla unnecessary to evaluate the final meter state in practice. After the process of pre-selection, interaction and post-selection, the final meter state takes the form,

$$\begin{aligned} & \frac{1}{\sqrt{N}} \left(\alpha\, |0\rangle + \beta \frac{\langle \psi_f |\, e^{-ikA}\, |\psi_i\rangle}{\langle \psi_f | \psi_i \rangle} |1\rangle \right) \qquad (2) \\ = \; & \frac{1}{\sqrt{N}} \left(\alpha\, |0\rangle + \beta A_m\, |1\rangle \right), \end{aligned}$$

where the value $\frac{1}{\sqrt{N}}$ is a normalization factor [6] and $\alpha\, |0\rangle + \beta\, |1\rangle$ is the meter initial state (prior to its interaction with the system of interest).

Modular values exhibit strong similarity to weak values under specific circumstances, particularly when k is small, so that the exponential can be approximated by using a Taylor expansion. Remarkably, the modular value represents a weak value of a unitary observable, when the unitary operator is also Hermitian. In recent years, both quantum weak values and modular values have garnered considerable attention due to their wide-ranging applications in various fields, such as quantum foundations [7, 8, 9, 10], quantum tomography [11, 12, 13], and particularly in quantum metrology [14, 15, 16, 17] and measurements [18, 19, 20, 21, 22, 23] in general. The intriguing quantum phenomena associated with weak and modular values hold significant promise for advancing our understanding of quantum mechanics and finding practical uses in cutting-edge technologies.

This paper introduces a novel approach to implementing quantum algorithms by leveraging the unique characteristics of modular values, in practice by calculating the modular value of the oracle involved in a quantum algorithm. Our proposed procedure capitalizes on the degrees of freedom inherent to modular values, including the fact that they are complex numbers. However, it is worth noting that this method necessitates the use of one extra qubit to facilitate the readout of the result obtained from the quantum modular value. The model can be applied to various algorithms. Our work bridges two captivating quantum research fields, whose links remained elusive, urging us to explore connections between quantum algorithms and weak and modular values.

While isolated studies have been conducted in this area [24], a comprehensive theoretical framework is yet to be established.

This paper is structured as follows. The initial section introduces a comprehensive approach to address quantum algorithms through modular values. Subsequently, these findings are applied to the distinct scenario associated with the Deutsch-Jozsa algorithm. Following this, we explore the diverse options for choosing adequately the pre- and post-selected states connected with the modular value. Furthermore, the outcomes of implementing this algorithm on an actual quantum computer—the IBM quantum computer—are showcased. Ultimately, the paper concludes by summarizing its contributions and outlining potential future directions.

1 Exploring the implementation of quantum algorithm via modular values of oracles

In this section, we provide a detailed procedure for tackling quantum algorithms using modular values. Our method involves carrying out a measurement with pre- and post-selection to the oracle. Oracles play a critical role in constructing algorithms in quantum computers [25, 26]. Essentially, an oracle is a black box that realizes unknown operations to the person executing the experiment. Oracles are implemented by using unitary operations and are commonly employed in quantum algorithms, such as the Deutsch-Jozsa algorithm and Grover's algorithm [1, 4].

As illustrated in Fig. 1, the complete quantum system used in our algorithm comprises $n+1$ qubits, with n qubits for executing the oracle (playing the role of the system of interest in the modular value measurement scheme) and one for the readout process (playing the role of the ancillary meter component). The algorithm consists of three main parts: (1) pre-selection of the oracle input state and preparation of the ancilla's state, (2) controlled oracle application, and (3) post-selection on the system to the final state and readout of the oracle to extract information related to the modular value. Finally, the measurement of the modular value unfolds by measuring the meter qubit (in case of successful post-selection).

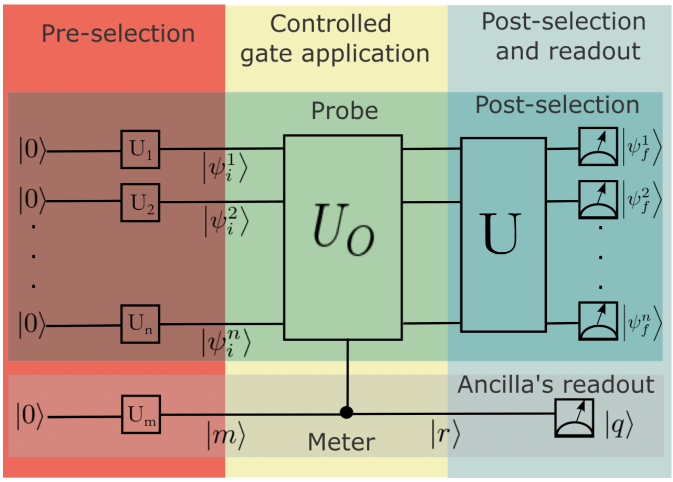

Figure 1: *The proposed model consists of n qubits plus a qubit meter that together form the full system. To prepare the system for the experiment, we first apply n unitary operators to the first n qubits to take them to the pre-selected state $|\psi_i\rangle$. We also use a unitary operator to set the qubit meter to its initial state. Next, we apply the controlled oracle to the system. To post-select, we apply additional unitary operators that could involve one or several qubits of the system. Finally, we measure the state of the full system in the computational basis, and the results of the joint measurement are then processed only on the condition of successful post-selection*

To begin, we take the oracle subsystem's n qubits to the pre-selected state

$$|\psi_i\rangle = \left|\psi_i^1\right\rangle \otimes |\psi_i^2\rangle \otimes ... \otimes |\psi_i^n\rangle \,, \tag{3}$$

by using unitary operators. The initial state of the meter, denoted as the projector $\hat{\Pi}_m$, is defined as

$$\hat{\Pi}_{\vec{m}} = \frac{1}{2}\left(\hat{I} + \vec{m}\cdot\hat{\vec{\sigma}}\right), \tag{4}$$

where $\vec{m}$ represents the state on the Bloch sphere, and $\hat{I}$ is the identity operator. To obtain this initial state, we employ a unitary operator.

Subsequently, we apply the following nonlocal unitary operator to the entire system, comprising the oracle subsystem and the meter:

$$\hat{U}_{\text{GATE}} = \hat{\Pi}_{\vec{r}} \otimes \hat{I} + \hat{\Pi}_{-\vec{r}} \otimes \hat{U}_O. \tag{5}$$

In this expression, $\hat{U}_O$ represents the oracle employed in the experiment, while $\hat{\Pi}_{\vec{r}}$ and $\hat{\Pi}_{-\vec{r}}$ are projectors applied to the ancillary space. These projectors can be expressed in terms of the vector $\pm\vec{r}$ on the Bloch sphere as follows:

$$\hat{\Pi}_{\pm\vec{r}} = \frac{1}{2}\left(\hat{I} \pm \vec{r}\cdot\hat{\vec{\sigma}}\right). \tag{6}$$

The unitary operator $\hat{U}_{\mathrm{GATE}}$ facilitates a controlled evolution of the oracle subsystem. When the ancillary projector is $\hat{\Pi}_{\vec{r}}$, the oracle subsystem does not evolve as it undergoes only the identity operation. Conversely, when the ancillary projector is $\hat{\Pi}_{-\vec{r}}$, the oracle subsystem experiences the application of the oracle operator $\hat{U}_O$. In the case of an ancillary state corresponding to a linear combination of these two scenarios, the superposed effect of both operators is applied to the oracle subsystem.

To complete the procedure, we post-select the oracle subsystem qubits to $|\psi_f\rangle$. Finally, by measuring the spin operator in the direction $\vec{q}$,

$$\hat{\sigma}_q = \hat{\Pi}_{+\vec{q}} - \hat{\Pi}_{-\vec{q}}, \tag{7}$$

we extract the information on the modular value upon successful post-selection. After some mathematical development shown in [27], the joint probabilities of finding the n qubits of the system in the composite state in $|\psi_f\rangle$ and the meter in $\pm q$ are computed from

$$P^{\pm\vec{q}}_{joint} = \mathrm{Tr}\left[\left(|\psi_f\rangle\langle\psi_f| \otimes \hat{\Pi}_{\pm\vec{q}}\right)\hat{\rho}\right], \tag{8}$$

where $\hat{\rho}$ is the state of the full system after the controlled application of the oracle. When applying the quantum eraser condition $\vec{r}\cdot\vec{q} = 0$ on the meter measurement basis[1], the joint probabilities take the form

$$\begin{aligned} P^{\pm\vec{q}}_{joint} &= \frac{1}{4}\{(1+\vec{r}\cdot\vec{m})\,|\langle\psi_f|\psi_i\rangle|^2 \qquad (9)\\ &+ (1-\vec{r}\cdot\vec{m})\,|\langle\psi_f|\,\hat{U}_O\,|\psi_i\rangle|^2\\ &\pm 2\,(\vec{m}\cdot\vec{q})\,\mathrm{Re}\left(\langle\psi_f|\,\hat{U}_O\,|\psi_i\rangle\langle\psi_i|\psi_f\rangle\right)\\ &\pm 2\,[(\vec{r}\times\vec{m})\cdot\vec{q}]\,\mathrm{Im}\left(\langle\psi_f|\,\hat{U}_O\,|\psi_i\rangle\langle\psi_i|\psi_f\rangle\right)\}. \end{aligned}$$

The expected value of the spin operator in the meter is [27],

$$\begin{aligned} \bar{\sigma}^m_q &= 2\frac{(\vec{m}\cdot\vec{q})\,\mathrm{Re}O_m + [(\vec{r}\times\vec{m})\cdot\vec{q}]\,\mathrm{Im}O_m}{(1+\vec{r}\cdot\vec{m}) + (1-\vec{r}\cdot\vec{m})\,|O_m|^2} \qquad (10)\\ &= \frac{P^{+\vec{q}}_{\mathrm{joint}} - P^{-\vec{q}}_{\mathrm{joint}}}{P^{+\vec{q}}_{\mathrm{joint}} + P^{-\vec{q}}_{\mathrm{joint}}}, \end{aligned}$$

where the modular value is

$$O_m = \frac{\langle\psi_f|\,\hat{U}_O\,|\psi_i\rangle}{\langle\psi_f|\psi_i\rangle}. \tag{11}$$

The qubit meter measurement extracts thus information on the modular value of the oracle, which in turn provides information relevant to solving the problem at hand, as will be illustrated in the following two sections. We note in particular that by choosing appropriate relative orientations of the meter directions $\vec{m}$, $\vec{r}$, and $\vec{q}$, it is possible to select the real of the imaginary part of the modular value in the numerator of expression (10).

In full generality, we can already state that to determine the required number of repetitions of the algorithm to obtain enough statistics to solve the initial problem, we need to evaluate the probability of post-selection, which is denoted at first order as

$$p = |\langle\psi_f|\psi_i\rangle|^2, \tag{12}$$

and the visibility that measures the contrast between joint probabilities that we measure, which is given by

$$V = \frac{P_{max} - P_{min}}{P_{max} + P_{min}}. \tag{13}$$

P_{min} represents the minimum joint probability between $P^{+\vec{q}}_{\mathrm{joint}}$ and $P^{-\vec{q}}_{\mathrm{joint}}$, while P_{max} corresponds to the maximum joint probability. In each particular case, the determination of the maximum and minimum joint probabilities is essential and can be achieved by considering the expression provided in Eq. 9. When employing this approach, there exist various degrees of freedom that can be optimized based on specific experimental conditions. These include selecting the pre- and post-selected states, choosing the meter state, and determining the operator to be measured in the meter. Additionally, alternative experimental approaches can be explored, which may lead to the emergence of modular values and the development of novel methods for executing quantum algorithms.

---

[1] Selecting two quantum states that are orthogonal on the Bloch sphere, expressed as $\vec{r}\cdot\vec{q} = 0$, maximizes the interference between different pathways during the meter measurement. In this configuration, the nonlocal gate action arises as a superposition of both $\hat{U}_O$ and $\hat{I}$, by causing a loss of information about the gate action. This particular circumstance is referred to as the "quantum eraser" condition, a term frequently employed in interferometer experiments to eliminate the knowledge of a particle's path. For instance, by applying a linear polarizer can erase the information regarding whether the polarization is circular left or right. All linear polarizations lie orthogonal on the Poincaré sphere to both left and right circular polarizations.

2 Standard quantum Deutsch-Jozsa algorithm

The Deutsch-Jozsa algorithm aims to determine whether a given function $f(x) : \{0,1\}^{n-1} \rightarrow \{0,1\}$ is constant or balanced. A constant function assigns the same value (either 0 or 1) to all the inputs, whereas a balanced function assigns the value 1 to exactly half of the inputs and the value 0 to the other half. Table 1 shows the different possibilities for the Deutsch-Jozsa algorithm for a function $f(x)$ with two-bit inputs (there are thus four possible inputs with two bits: 00, 01, 10, and 11).

Balanced

$f(00)$	$f(01)$	$f(10)$	$f(11)$
0	0	1	1
0	1	0	1
0	1	1	0
1	1	0	0
1	0	1	0
1	0	0	1

Constant

$f(00)$	$f(01)$	$f(10)$	$f(11)$
0	0	0	0
1	1	1	1

Table 1: *All the possible combinations of two-bit inputs and single-bit outputs that result in either a constant or a balanced function.*

In 1992, Deutsch and Jozsa introduced a groundbreaking quantum circuit that solves this problem in a single step, providing a significant advantage over the classical counterpart. In the worst-case scenario, the classical approach requires 2^{n-1} repetitions, where 2^{n-1} represents the total number of different inputs for the function. However, by leveraging qubits, we can exploit the fact that 2^{n-1} corresponds to the dimensionality of the space formed by $n-1$ qubits. Thus, we can effectively employ $n-1$ qubits to generate the entire set of 2^{n-1} inputs. In stark contrast to classical approaches, the quantum circuit designed by Deutsch and Jozsa achieves the same result efficiently. The quantum circuit is depicted in Fig. 2, showcasing its elegance and simplicity. To tackle the problem with 2^{n-1} inputs, the algorithm mandates the utilization of n qubits. To address a problem involving a function with all possible combinations of $n-1$ qubits as input, it is necessary to utilize a total of n qubits. The first $n-1$ qubits are initialized in the state $|0\rangle$, while the remaining qubit is initialized in the state $|1\rangle$. This initialization results in the following state:

$$|\psi_0\rangle = |0\rangle^{\otimes(n-1)} |1\rangle \tag{14}$$

where $|0\rangle^{\otimes(n-1)}$ is a compact notation for the tensor product of $n-1$ state kets $|0\rangle$, i. e. $|0\rangle \otimes |0\rangle \ldots \otimes |0\rangle$, and the basis has been chosen as

$$|0\rangle = \begin{pmatrix} 1 \\ 0 \end{pmatrix} \qquad |1\rangle = \begin{pmatrix} 0 \\ 1 \end{pmatrix}. \tag{15}$$

The first step consists of applying the Hadamard gate, $\hat{H}$,

$$\hat{H} = \frac{1}{\sqrt{2}} \begin{pmatrix} 1 & 1 \\ 1 & -1 \end{pmatrix} \tag{16}$$

to all $n-1$ qubits. The state after the transformation is

$$\begin{aligned} |\psi_1\rangle &= \frac{1}{\sqrt{2^n}} \left(|0\rangle + |1\rangle\right)^{\otimes n-1} \left(|0\rangle - |1\rangle\right) \quad (17) \\ &= \sum_{x\in\{0,1\}^{n-1}} \frac{1}{\sqrt{2^n}} |x\rangle \left(|0\rangle - |1\rangle\right), \end{aligned}$$

where $|x\rangle$ are all the 2^{n-1} states of the basis with $n-1$ qubits.

After applying the Hadamard gates, the oracle is applied to the n qubits. The oracle acts as

$$\hat{U}_f |x, y\rangle \rightarrow |x, y \oplus f(x)\rangle, \tag{18}$$

where $\oplus$ represents the addition modulo 2, that is 0 if both terms are equal and 1 if both terms are different

$$\begin{aligned} 0 \oplus 0 &= 0 \quad (19) \\ 0 \oplus 1 &= 1 \\ 1 \oplus 0 &= 1 \\ 1 \oplus 1 &= 0. \end{aligned}$$

The resulting state after the application of the oracle is:

$$\begin{aligned} |\psi_2\rangle &= \sum_{x\in\{0,1\}^{n-1}} \frac{1}{\sqrt{2^n}} |x\rangle \left(|0 \oplus f(x)\rangle - |1 \oplus f(x)\rangle\right) \\ &= \sum_{x\in\{0,1\}^{n-1}} \frac{(-1)^{f(x)}}{\sqrt{2^n}} |x\rangle \left(|0\rangle - |1\rangle\right). \quad (20) \end{aligned}$$

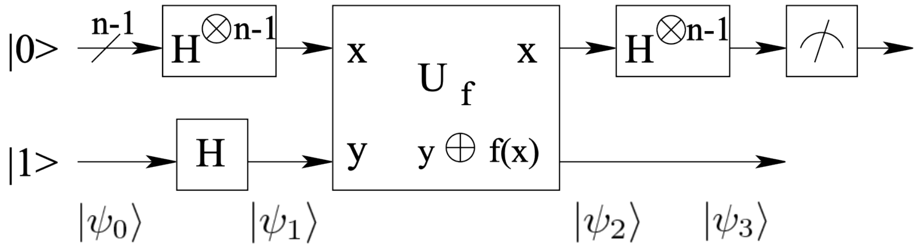

Figure 2: *Deutsch-Jozsa quantum circuit, where U_f is the oracle, H is the Hadamard gate, and the states $|\psi_0\rangle$, $|\psi_1\rangle$, $|\psi_2\rangle$, and $|\psi_3\rangle$ are detailed in the text. Modified from Peplm, https://commons.wikimedia.org/wiki/File:Deutsch-Jozsa-algorithm-quantum-circuit.png, accessed on the 9th of May 2023.*

In Eq. 20, we make use of the property that $|0 \oplus f(x)\rangle = |f(x)\rangle$, while $|1 \oplus f(x)\rangle = |1 - f(x)\rangle$.

Subsequently, Hadamard gates, denoted as $\hat{H}^{\otimes(n-1)}$, are applied to the first $n-1$ qubits. The application of $n-1$ Hadamard gates to an $n-1$-qubit state can be expressed as:

$$\hat{H}^{\otimes n-1} |x_1, \ldots, x_{n-1}\rangle \tag{21}$$
$$= \frac{\sum_{z_1,\ldots,z_{n-1}} (-1)^{x_1 z_1 + \ldots + x_{n-1} z_{n-1}} |z_1, \ldots, z_{n-1}\rangle}{\sqrt{2^{n-1}}},$$

where x_i are the components of the state $|x\rangle$, while z_i are the ones of the state $|z\rangle$, hence every component is either a 0 or a 1.

The notation can be simplified as

$$\hat{H}^{\otimes(n-1)} |x\rangle = \frac{\sum_z (-1)^{x \cdot z} |z\rangle}{\sqrt{2^{n-1}}}, \tag{22}$$

where $x \cdot z$ is the inner product of x and z, modulo 2. Finally, the state $|\psi_3\rangle$ is obtained after applying the Hadamard gate to the first $n-1$ qubits,

$$|\psi_3\rangle = \sum_{z_1,\ldots,z_{n-1}} \sum_{x_1,\ldots,z_{n-1}} \frac{1}{\sqrt{2^n}} (-1)^{x \cdot z + f(x)} |z\rangle (|0\rangle - |1\rangle) \tag{23}$$

Eventually, if we measure in the $\{|0\rangle, |1\rangle\}^{n-1}$ basis the $n-1$ first qubits, the probability of obtaining the state $|0\rangle^{\otimes(n-1)}$ would be,

$$\left| \frac{1}{2^{n-1}} \sum_{x=0}^{2^{n-1}-1} (-1)^{f(x)} \right|. \tag{24}$$

Consequently, if the measurement result is $|0\rangle^{\otimes(n-1)}$, the function is constant, whereas if the measurement result is different from $|0\rangle^{\otimes(n-1)}$, the function is balanced. By applying the algorithm once, we can determine with certainty whether the function is balanced or constant.

Although the Deutsch-Jozsa algorithm does not have any real-world applications, it was one of the first quantum algorithms to demonstrate a clear advantage over its classical counterpart.

3 Deutsch-Jozsa-inspired algorithm by using modular values

In the previous section, we discussed the conventional method for solving the Deutsch-Jozsa problem. In this section, we explore an alternative approach by calculating the modular value of the standard oracle operator $\hat{U}_O$. When solving the problem with 2^{n-1} possible inputs, the oracle is applied to n qubits. As a result, the pre- and post-selected states in our procedure correspond to n-qubit states. To extract the modular value, an additional qubit, known as the ancilla qubit, is required. Therefore, a total of $n+1$ qubits are needed in our approach. The application of the oracle can be expressed as

$$\hat{U}_O (|x\rangle |y\rangle) = |x\rangle |y \oplus f(x)\rangle. \tag{25}$$

The algorithm can be implemented by calculating the modular value of the oracle in systems of any dimension.

The Deutsch-Jozsa problem for a function of 4 different inputs (all possible values of two bits) requires two qubits for the oracle, and thus three qubits in total in order to evaluate the modular value of the oracle, as seen in the previous section. In the modular value approach, the oracle subsystem spans thus two qubits, while we need an extra qubit to act as the ancilla. With these dimensions, the chosen pre- and post-selected states are:

$$
\begin{aligned}
|\psi_i\rangle &= \frac{1}{\sqrt{8}}\left(|0\rangle+|1\rangle\right)\otimes\left(|0\rangle+|1\rangle\right) \qquad (26)\\
&\otimes \left(|0\rangle-|1\rangle\right)\\
&= \frac{1}{\sqrt{8}}(|000\rangle+|010\rangle+|100\rangle+|110\rangle\\
&- |001\rangle-|011\rangle-|101\rangle-|111\rangle)\\
|\psi_f\rangle &= \frac{1}{\sqrt{11}}(-2i\,|000\rangle-i\,|010\rangle+i\,|001\rangle\\
&+ i\,|011\rangle+|100\rangle+|110\rangle-|101\rangle-|111\rangle).
\end{aligned}
$$

The probability of post-selection in this case is given by $p = |\langle\psi_f|\psi_i\rangle|^2 = \frac{41}{88} \approx 0.47$, which is slightly below one-half. Consequently, on average, two attempts are needed to achieve successful post-selection. When the function $f(x) : \{0,1\}^{n-1} \rightarrow \{0,1\}$ is constant, meaning that $f(x)$ is either 0 or 1 for all x, the numerator of the modular value is equal to the denominator or its opposite. Thus, the modular value is either 1 or -1, resulting in a purely real value. On the other hand, when the function $f(x) : \{0,1\}^n \rightarrow \{0,1\}$ is balanced, with half of the terms $f(x)$ equal to 1 and the other half equal to 0, the modular values possess an imaginary part for all possible balanced combinations of $f(x)$.

In Table 2, all balanced possibilities using three qubits (two qubit inputs and one ancilla) are presented. All modular values have an imaginary part, which allows for discrimination between balanced and constant functions by measuring this part. This process is easily generalized to the algorithm with $n+1$ qubits (the n qubits of the Deutsch-Jozsa algorithm plus the ancilla). In this case, the pre-selected state is the natural generalization of the previous case

$$|\psi_i\rangle = \frac{1}{\sqrt{2^n}}\left(|0\rangle+|1\rangle\right)^{\otimes(n-1)}\left(|0\rangle-|1\rangle\right). \qquad (27)$$

The post-selected state is generalized from the three-qubit case,

$$
\begin{aligned}
|\psi_f\rangle &= \frac{1}{\sqrt{2^n+3}}(-2i\,|00...0\rangle+i\,|00...0...01\rangle \qquad (28)\\
&+ (-i\sum_{j=2}^{2^{n-2}} \underbrace{\left|0a_2...a_{(2^{n-1})}\right\rangle_j}_{\substack{(2^{n-1})/2-1 \text{ first terms with } n-1\\ \text{qubits without including } |000...0\rangle}}\\
&+ \sum_{k=2^{n-2}+1}^{2^{n-1}} \underbrace{\left|1b_2...b_{(2^{n-1})}\right\rangle_k}_{(2^{n-1})/2 \text{ last terms with } n-1 \text{ qubits}} \quad)\\
&\times (|0\rangle-|1\rangle))
\end{aligned}
$$

The probability of post-selection using the states Eq. 27 and Eq. 28 is

$$p = \frac{2^n\left(1+2^{n-1}\right)+1}{2^n\left(3+2^n\right)} = \frac{2^{2n-1}+2^n+1}{2^{2n}+3\times 2^n}, \qquad (29)$$

whose limit when n tends to infinity is $\frac{1}{2}$. Therefore, on average, two attempts are required for successful post-selection. In the case where the function $f(x) : \{0,1\}^{n-1} \rightarrow \{0,1\}$ is constant, the numerator and denominator of the modular value take the same value or the opposite value, resulting in a modular value of either 1 or -1. Conversely, when the function is balanced, the modular value presents always an imaginary part. Discrimination between a real and complex modular value can be accomplished by selecting appropriate measurement directions (i.e., vector $\vec{q}$) for the ancillary component. Indeed, the measurement results provided by Eq. 10 depend on both the real and imaginary parts of the modular value. However, by choosing vectors $\vec{m}$ and $\vec{q}$ that are perpendicular, the real part does not contribute to the numerator (because $\vec{m}\cdot\vec{q} = 0$ in Eq. 10), so that a non-zero measurement result indicates that the modular value possesses a non-zero imaginary part. Conversely, by choosing vectors such that $(\vec{r}\times\vec{m})\cdot\vec{q} = 0$, only the real part contributes to the numerator providing the measurement results. Furthermore, through the meticulous selection of appropriate pre- and post-selected states, one can ascertain the specific way in which the function is balanced among the various possibilities (each row of the balanced table in Table 1). In such cases, the modular value associated with the oracle would vary for each distinct manner of achieving a balanced function, corresponding to each row in the balanced table presented in Table 1.

$f(00)$	$f(01)$	$f(10)$	$f(11)$	O_m	$\mathrm{Re}\,(O_m)$	$\mathrm{Im}\,(O_m)$
0	0	1	1	$\frac{5i-4}{5i+4}$	$\frac{9}{41}$	$\frac{40}{41}$
0	1	0	1	$\frac{i}{5i+4}$	$\frac{5}{41}$	$\frac{4}{41}$
0	1	1	0	$\frac{i}{5i+4}$	$\frac{5}{41}$	$\frac{4}{41}$
1	1	0	0	$\frac{-5i+4}{5i+4}$	$-\frac{9}{41}$	$-\frac{40}{41}$
1	0	1	0	$\frac{-i}{5i+4}$	$-\frac{5}{41}$	$-\frac{4}{41}$
1	0	0	1	$\frac{-i}{5i+4}$	$-\frac{5}{41}$	$-\frac{4}{41}$

Table 2: *All the possible combinations to have a balanced function with three qubits and the corresponding modular values.*

4 Choice of pre- and post-selected states in the Deutsch-Jozsa-inspired algorithm by using modular values

In the previous section, we introduced the pre- and post-selected states for solving the Deutsch-Jozsa problem using modular values, as described in Eq. 27 and Eq. 28. However, one might question the rationale behind this particular choice. Our objective is to find two quantum states (pre-selected and post-selected) that yield a non-zero imaginary part of the weak value of the oracle for all possible balanced functions $f(x)$, as given in Table 1. Ideally, we aim to maximize this imaginary part while minimizing the real part of the modular value, in order to enhance the visibility defined in Eq. 13. Additionally, we strive to maximize the probability of successful post-selection. Hence, we are confronted with an optimization problem.

In order to explore the entire quantum space, we conducted a random mapping of the complete state space for the pre-selected and post-selected states, both consisting of four-level states (two qubits). The pseudorandom numbers used were integer values drawn from a discrete uniform distribution. Fig. 3 showcases the resulting average visibility of all combinations of the balanced function, which are further detailed in Table 1, as a function of the probability of post-selection. In this particular case, we have chosen to focus on separable states, as they are easier to generate using quantum gates, such as those available in the IBM quantum computer. As depicted in the plot, there is a trade-off that needs to be considered. On one hand, we can achieve a very high probability of post-selection, but at the cost of lower visibility. On the other hand, we can enhance the visibility, but with a decrease in the probability of successful post-selection.

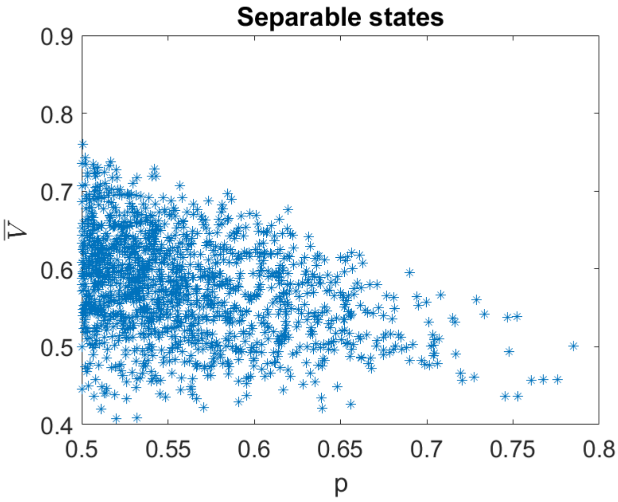

Figure 3: *Average visibility as a function of the probability of post-selection in the Deutsch-Jozsa problem for the 2 qubits case. All pre- and post-selected states are separable two-qubit states and are generated randomly. Our criteria for selecting these states were to ensure that, for each balanced function, the imaginary part of the weak value of the oracle is greater than* 0.1*, each individual visibility is greater than* 0.4*, and the probability of post-selection is greater than* 0.5*. By imposing these conditions, we aim to strike a balance between a high post-selection probability, and strong visibility to ensure the ability to distinguish between constant and balanced functions.*

Alternatively, we can explore the space of non-separable states (including separable ones) as a potential solution. In Fig. 4, we present a denser plot where we consider both separable and non-separable states. This broader range of states offers more possibilities for achieving intermediate values of average visibility in relation to the probability of post-selection. It was expected that including non-separable states would

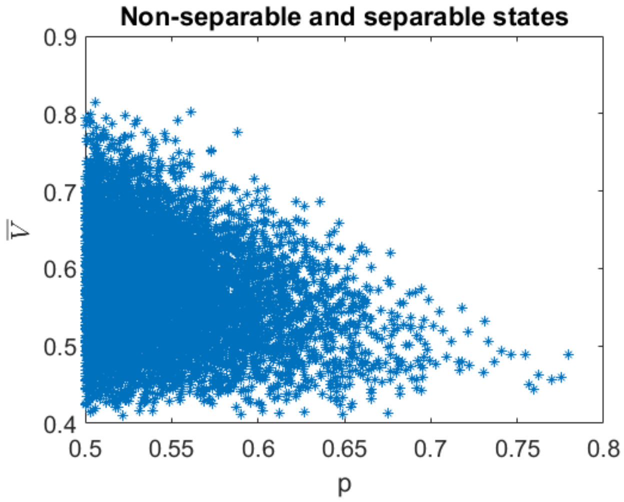

Figure 4: *Average visibility as a function of the probability of post-selection in the Deutsch-Jozsa problem for the 2 qubits case. All pre- and post-selected states are generated randomly without constraint (a typical state will thus be non-separable). Average visibility in terms of the probability of post-selection for randomly generated two-qubit non-separable and separable pre- and post-selected states in the context of the Deutsch-Jozsa problem. For this analysis, we have imposed a minimum threshold of* 0.1 *for the imaginary part of each weak value of the oracle, considering all balanced functions. Additionally, each individual visibility is required to exceed* 0.4, *and the probability of post-selection must be greater than* 0.5.

provide additional options beyond the separable ones. When aiming for low visibility (around 0.4) and high post-selection probability (around 0.8), the benefit of incorporating non-separable states is limited. However, when targeting a lower probability of post-selection (around 0.5), we observe points on the plot that yield improved average visibility values exceeding 0.8. Interestingly, we observe the emergence of a distinct trend in the form of a dividing line, which seems to move up when non-separable states are considered. This suggests that there is a clear boundary beyond which points are not found above the line. It is worth noting that by choosing non-separable states introduces additional complexity in generating such states on a quantum computer. This typically involves utilizing multi-qubit gates such as the CNOT or the TOFFOLI gates. Despite the challenges involved, non-separable states offer potential advantages, as demonstrated by the improved average visibility and probability of post-selection in certain regions of the plot. Given the trade-off between selecting separable and non-separable states, we opted for simplicity in the implementation of the Deutsch-Jozsa problem on the IBM quantum computer in the subsequent section. We specifically chose straightforward pre- and post-selected states that enable differentiation between only one particular balanced function, and constant functions. This decision was motivated by the difficulty of implementing more complex states using the available gates.

5 Implementation of the the Deutsch-Jozsa-inspired algorithm by using modular values in the IBM quantum computer

To experimentally implement our algorithm tackling the Deutsch-Jozsa problem, we can follow the scheme shown in Fig. 1. In this approach, we need to select the initial state of the meter, denoted by $|m\rangle$ (Eq. 4), the projectors $\hat{\Pi}_{\pm\vec{r}}$ (Eq. 6), and the final state measured in the meter, denoted by $|q\rangle$ (Eq. 7). We should impose $\vec{r}\cdot\vec{q}=0$ to satisfy the quantum eraser condition. Additionally, we choose to enforce $\vec{m}\cdot\vec{q}=0$ in order to have direct access to the imaginary part of the modular value (see Eq. 10). The initial meter state corresponds thus to

$$\hat{\Pi}_{\vec{m}}=\frac{1}{2}\left(\hat{I}+\hat{\sigma}_z\right), \tag{30}$$

where $\vec{m}=(0,0,1)$. The projector controlling the application of the oracle is

$$\hat{\Pi}_{\vec{r}}=\frac{1}{2}\left(\hat{I}+\hat{\sigma}_x\right), \tag{31}$$

where $\vec{r}=(1,0,0)$. The observable to measure in the meter is $\hat{\sigma}_y$, with $\vec{q}=(0,1,0)$.
Applying the selected states, the average measured value of $\hat{\sigma}_y$ in the probe is

$$\bar{\sigma}_y^m=\frac{-2\,\mathrm{Im}\left(O_m\right)}{1+|O_m|^2}. \tag{32}$$

Taking into account the joint probability values in this scenario, the visibility is given by

$$V=\frac{2\,|\mathrm{Im}\left(O_m\right)|}{1+|\mathrm{Im}\left(O_m\right)|^2+|\mathrm{Re}\left(O_m\right)|^2}. \tag{33}$$

It is desirable to achieve a high visibility to distinguish in fewer repetitions of the experiment the real part from the imaginary one. In particular, the maximum visibility $V = 1$ is reached for $\mathrm{Im}\left(O_m\right) = \pm 1$ and $\mathrm{Re}\left(O_m\right) = 0$. The closer the real part to 0, the better; the closer the absolute value of the imaginary part to 1, the better. This is equivalent to maximizing $\frac{2x}{x^2+y^2+1}$ with respect to x and y. For the case of the Deutsch-Jozsa problem with two qubits, $f\left(x\right) : \{0,1\}^2 \to \{0,1\}$ shown in Table 2, the first and third possibilities to balance the system have a good visibility, while the others do not. These values can be optimized at the expense of losing some visibility on the first and third cases. The number of times the algorithm should be executed, named shots in the jargon, depends on the level of uncertainty one is willing to accept.

We ran the modular value algorithm to solve the Deutsch-Jozsa problem on the Quito IBM quantum computer (ibmq_quito), by using modular values, for one constant and one balanced case. The pre-selected state is chosen as described in Eq. 26, and we simplified the post-selected state by choosing it as follows

$$\begin{aligned}\left|\psi_f\right\rangle &= \frac{1}{\sqrt{8}}(\left|000\right\rangle + \left|010\right\rangle + i\left|100\right\rangle \\ &+ i\left|110\right\rangle - \left|001\right\rangle - \left|011\right\rangle - i\left|101\right\rangle - i\left|111\right\rangle).\end{aligned} \tag{34}$$

The latter state has been chosen, because it can be easily obtained through simple gates on the IBM quantum computer. Let us however observe that in this case, only one type of balanced function can be discriminated from the constant case, namely a single raw in the top Table 1. In a next step, it would be desirable to implement the post-selected state expressed in Eq. 26. The probability of post-selection by using the state described in Eq. 34 is $p = \frac{1}{2}$. The states $\left|m\right\rangle$, $\left|r\right\rangle$, and $\left|q\right\rangle$ were chosen as described earlier.

The circuit applied when the function was constant is shown in Fig. 5, where no gate was used to create the oracle, as the circuit is constant, mathematically represented by the identity operator, $\hat{I}$. The unitary operators present in Fig. 5 are used to post-select. They are defined as

$$\hat{U}\left(\theta,\phi,\lambda\right) = \begin{pmatrix} \cos\frac{\theta}{2} & -e^{-i\lambda}\sin\frac{\theta}{2} \\ e^{i\phi}\sin\frac{\theta}{2} & e^{\phi+\lambda}\cos\frac{\theta}{2} \end{pmatrix}. \tag{35}$$

Basically, we associate the post-selected state to the result $\left|000\right\rangle$, which implies that finding the system in that state would be equivalent to having post-selected on the state $\left|\psi_f\right\rangle$. The circuit applied when the function is balanced, with $f\left(00\right) = f\left(01\right) = 0$ and $f\left(10\right) = f\left(11\right) = 1$, is shown in Fig. 6. The modular value is equal to 1 when the function is constant, with $\hat{\sigma}_y^m = 0$, and equal to i when the function is balanced, with $\hat{\sigma}_y^m = -1$. The visibility was 1 for the balanced case and 0 for the constant case.

Fig. 7 and Fig. 9 portray the averages of the outcomes of the $\hat{\sigma}_y$ measurements required to solve the Deutsch-Jozsa problem within the framework of the modular-value algorithm, when executed on the IBM Quito quantum computer (ibmq_quito) and on the IBM simulator_mps (ibmq_simulator_mps). These results are exhibited as a function of the repetition count. Correspondingly, Fig. 8 and Fig. 10 present the post-selection rates for both the balanced and constant cases run in the quantum computer and in a simulator. It is noteworthy that the theoretical post-selection probability stands at first order at $\frac{1}{2}$, while the value computed through the IBM quantum simulator reaches 0.51. In the ibmq_quito, the post-selection rate varies between 0.4 and 0.6, while in the simulator (no errors are involved), the post-selected rate fluctuates much less, between 0.47 and 0.53. The determination of the requisite number of repetitions is contingent upon the desired data quality and the precision of the experimental setup. Remarkably, the distinction between the two cases—constant and balanced—was successfully accomplished with 32 shots, incorporating unsuccessful post-selections as well. A pivotal observation is that the ibmq_quito system is markedly influenced by substantial noise, as evidenced by a median CNOT error of 6.895e-3 and a median readout error of 3.920e-2. If no errors were involved in the quantum computer, 8 shots would be enough to differentiate between balanced and constant, as we can see in Fig. 9. It is worth emphasizing that this procedure can also be conducted utilizing alternative experimental configurations, such as optical systems.

6 Conclusions and perspectives

We have introduced a novel approach for executing quantum algorithms by using modular values. This technique is applicable to various quantum

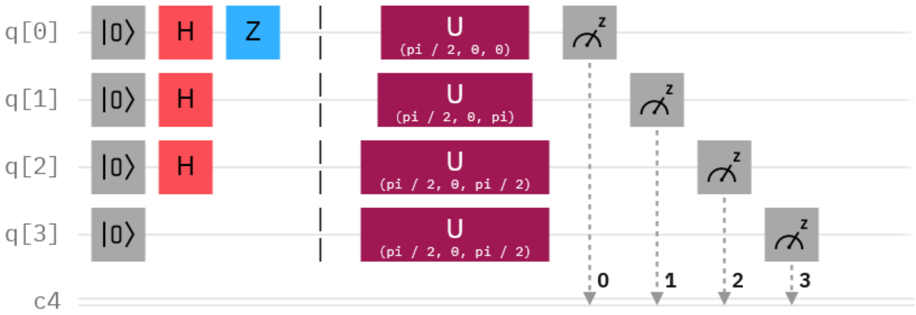

Figure 5: *Circuit diagram for the modular value algorithm for the Deutsch-Jozsa problem with a constant function using* 3 *qubits and one ancilla qubit. The circuit applies the unitary operator* $\hat{U}\left(\frac{\pi}{2},0,0\right)$ *to qubit* 0, $\hat{U}\left(\frac{\pi}{2},0,\pi\right)$ *to qubit* 1, $\hat{U}\left(\frac{\pi}{2},0,\frac{\pi}{2}\right)$ *to qubit* 2, *and* $\hat{U}\left(\frac{\pi}{2},0,\frac{\pi}{2}\right)$ *to qubit* 3. *Figure produced with https://quantum-computing.ibm.com.*

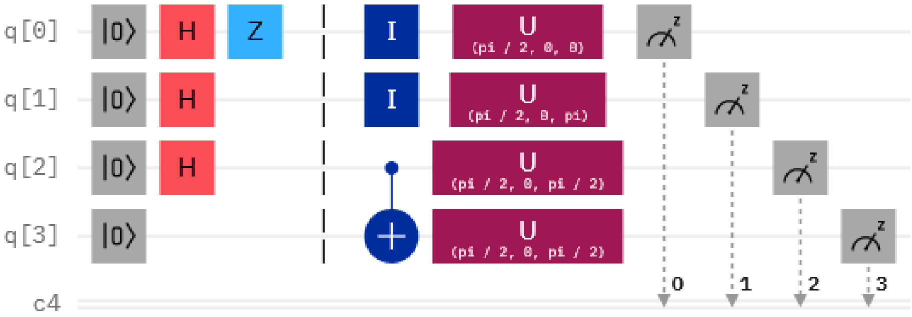

Figure 6: *The circuit diagram illustrates the implementation of the modular value algorithm for the Deutsch-Jozsa problem for the balanced case, using a 3-qubit system and one ancilla qubit. The gates applied to each qubit are* $\hat{U}\left(\pi/2,0,\pi\right)$ *to qubit* 0, $\hat{U}\left(\pi/2,0,\pi\right)$ *to qubit* 1, $\hat{U}\left(\pi/2,0,\pi/2\right)$ *to qubit* 2, *and* $\hat{U}\left(\pi/2,0,\pi/2\right)$ *to qubit* 3. *Figure produced with https://quantum-computing.ibm.com.*

algorithms that involve an oracle. An additional qubit is needed to read out the modular value result. The number of shots required depends on the post-selection probability and visibility. This procedure can be applied to different experimental setups such as quantum computers or optical systems.

This paper presents a method for implementing algorithms by using modular values in quantum computers. Despite the considerable noise in the ibmq_quito quantum computer, with errors on the order of 10^{-3} for quantum gates and 10^{-2} for measuring, we have achieved preliminary results for the Deutsch-Jozsa problem by using modular values. No advantages were observed in that particular case. It requires a significantly larger number of shots compared to the standard algorithm, where only one shot is typically sufficient (if no errors are considered). While there are various ways to potentially improve the algorithm, such as selecting appropriate pre- and post-selected states, it is unlikely to yield any significant advantages in this scenario. The probability of post-selection consistently hinders the efficiency of the modular value-based algorithm in reaching the correct result expeditiously.

The modular value-based approach demonstrates significant potential as a more precise alternative to various algorithms. For instance, in the Deutsch-Jozsa algorithm, it can discern between the various manners of achieving a balanced function. Moreover, this method could also facilitate the development of new algorithms provided a quantitative validation is performed.

In general, we have not yet found any experimental computational advantage over conventional quantum algorithms. Several questions need to be addressed to explore this approach further. First, we need to study all the information provided by the measurements in the computational basis to reduce the number of shots required. Post-selection in the different states of the computational basis simultaneously could be a possible approach, as we directly obtain the information when running an

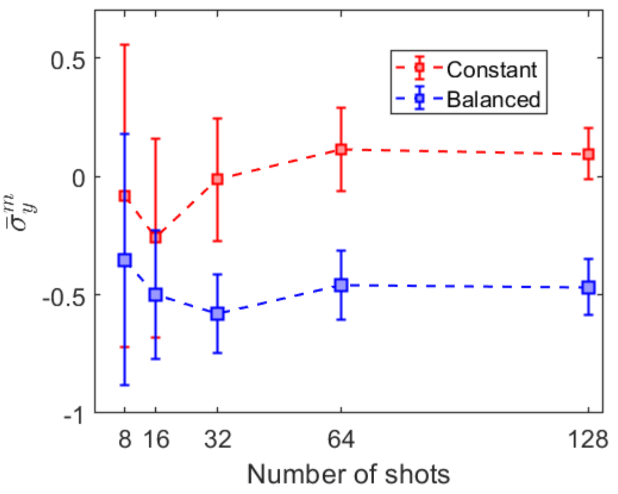

Figure 7: *Mean* $\hat{\sigma}_y$ *operator measurement outcomes for both the constant and balanced cases across a range of shots (8, 16, 32, 64, and 128): experiment run in the ibmq_quito quantum computer. The entire procedure has been iterated a total of 12 times for each distinct run count. Furthermore, to provide a comprehensive representation, the standard deviation has been incorporated in the form of error bars.*

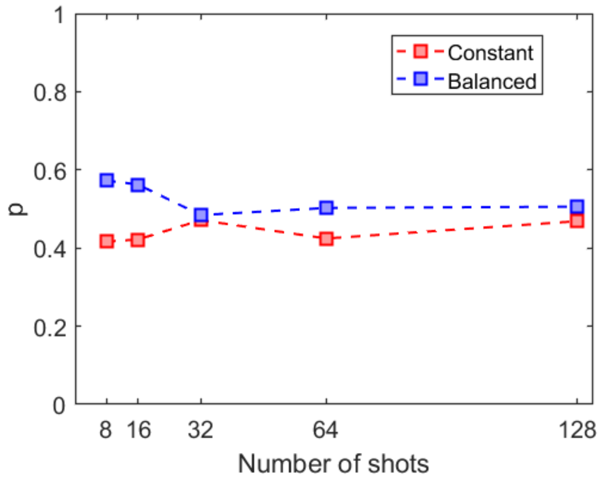

Figure 8: *Experimental average post-selection rate, p, for varying number of shots: 8, 16, 32, 64, and 128, encompassing both the constant and balanced scenarios. Experiment run in the ibmq_quito quantum computer.*

algorithm on a quantum computer. Additionally, we need to investigate the selection of pre- and post-selected states to increase the algorithm's efficiency, specifically by examining the states' separability. As we have seen, non-separable states provide a larger parameter space. However, these states are much more complicated to create by using the common quantum gates. Separable states can be created by using an individual unitary transformation in each qubit. This approach is not always possible for non-separable states. From a computational perspective, we need to improve our ability to create non-separable states by using standard gates.

Finally, modular values are expected to yield

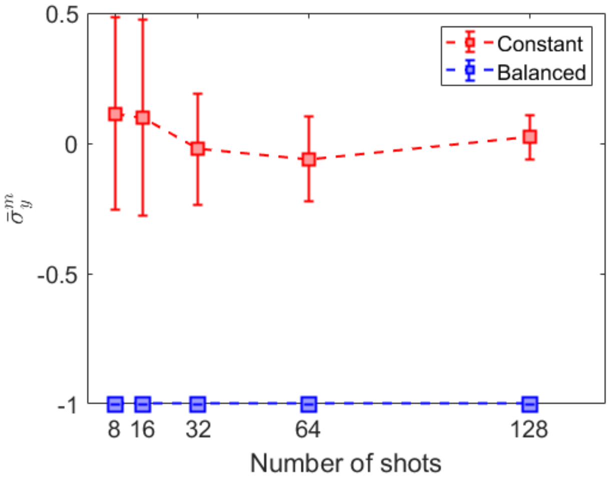

Figure 9: *Mean* $\hat{\sigma}_y$ *operator measurement outcomes for both the constant and balanced cases across a range of shots (8, 16, 32, 64, and 128): experiment run in the IBM simulator_mps. The entire procedure has been iterated a total of 12 times for each distinct run count. Furthermore, to provide a comprehensive representation, the standard deviation has been incorporated in the form of error bars.*

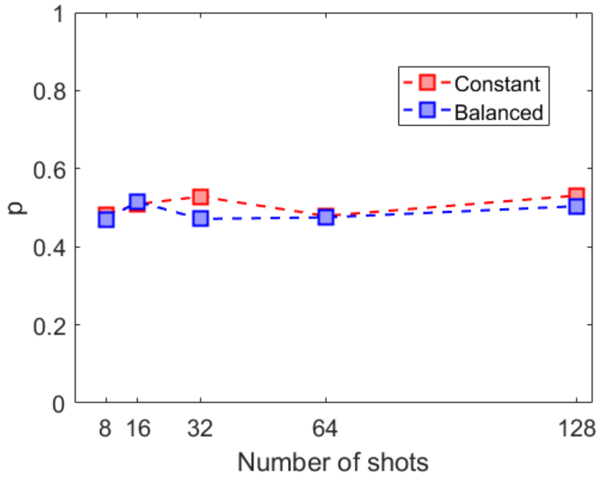

Figure 10: *Experimental average post-selection rate, p, for varying number of shots: 8, 16, 32, 64, and 128, encompassing both the constant and balanced scenarios. Experiment run in the IBM simulator_mps.*

good results in algorithms that search for small quantities due to their amplification capability. For example, we could differentiate between two almost identical gates. Even though, in that case, the probability of post-selection would be very small, the precision that one can reach by using a modular value-based approach could be better than by using other standard approaches, at least in the presence of technical limitations. In the counterpart, the required number of repetitions of the algorithm could be very large.

In summary, exploring the applicability of modular values in various contexts could yield valuable insights and advancements in the field of quantum computing.

Acknowledgments

Y.C. is a research associate of the Fund for Scientific Research (F.R.S.-FNRS). This research was supported by the Action de Recherche Concertée WeaM at the University of Namur (19/23-001). We acknowledge the use of IBM Quantum services for this work. The views expressed are those of the authors and do not reflect the official policy or position of IBM or the IBM Quantum team.

References

[1] Lov K Grover. A fast quantum mechanical algorithm for database search. In *Proceedings of the twenty-eighth annual ACM symposium on Theory of computing*, pages 212–219, 1996.

[2] Peter W Shor. Algorithms for quantum computation: discrete logarithms and factoring. In *Proceedings 35th annual symposium on foundations of computer science*, pages 124–134. Ieee, 1994.

[3] David Deutsch and Richard Jozsa. Rapid solution of problems by quantum computation. *Proceedings of the Royal Society of London. Series A: Mathematical and Physical Sciences*, 439(1907):553–558, 1992.

[4] Richard Cleve, Artur Ekert, Chiara Macchiavello, and Michele Mosca. Quantum algorithms revisited. *Proceedings of the Royal Society of London. Series A: Mathematical, Physical and Engineering Sciences*, 454(1969):339–354, 1998.

[5] Yakir Aharonov, David Z Albert, and Lev Vaidman. How the result of a measurement of a component of the spin of a spin-1/2 particle can turn out to be 100. *Physical review letters*, 60(14):1351, 1988.

[6] Yaron Kedem and Lev Vaidman. Modular values and weak values of quantum observables. *Physical review letters*, 105(23):230401, 2010.

[7] Sacha Kocsis, Boris Braverman, Sylvain Ravets, Martin J Stevens, Richard P Mirin, L Krister Shalm, and Aephraim M Steinberg. Observing the average trajectories of single photons in a two-slit interferometer. *Science*, 332(6034):1170–1173, 2011.

[8] A Matzkin. Weak values and quantum properties. *Foundations of Physics*, 49(3):298–316, 2019.

[9] E Rafiepoor, M R Bazrafkan, and S Batebi. The nonclassicality of a quantum system in weak measurement by means of modular values. *J. Mod. Opt.*, 68(5):295–301, March 2021.

[10] Mirko Cormann and Yves Caudano. Geometric description of modular and weak values in discrete quantum systems using the majorana representation. *J. Phys. A Math. Theor.*, 50(30):305302, June 2017.

[11] Jeff S Lundeen, Brandon Sutherland, Aabid Patel, Corey Stewart, and Charles Bamber. Direct measurement of the quantum wavefunction. *Nature*, 474(7350):188–191, June 2011.

[12] Wei-Wei Pan, Xiao-Ye Xu, Yaron Kedem, Qin-Qin Wang, Zhe Chen, Munsif Jan, Kai Sun, Jin-Shi Xu, Yong-Jian Han, Chuan-Feng Li, and Guang-Can Guo. Direct measurement of a nonlocal entangled quantum state. *Phys. Rev. Lett.*, 123(15), October 2019.

[13] Yusuf Turek. Direct measurement methods of density matrix of an entangled quantum state. *J. of Phys. Commun.*, 4(7):075007, July 2020.

[14] Onur Hosten and Paul Kwiat. Observation of the spin hall effect of light via weak measurements. *Science*, 319(5864):787–790, 2008.

[15] Lijian Zhang, Animesh Datta, and Ian A Walmsley. Precision metrology using weak measurements. *Physical review letters*, 114(21):210801, 2015.

[16] Dongmei Li, Tian Guan, Yonghong He, Fang Liu, Anping Yang, Qinghua He, Zhiyuan Shen, and Meiguo Xin. A chiral sensor based on weak measurement for the determination of proline enantiomers in diverse measuring circumstances. *Biosensors and Bioelectronics*, 110:103–109, 2018.

[17] Le Bin Ho and Yasushi Kondo. Modular-value-based metrology with spin coherent pointers. *Phys. Lett. A*, 383(2-3):153–157, January 2019.

[18] Le Bin Ho and Nobuyuki Imoto. Full characterization of modular values for finite-dimensional systems. *Phys. Lett. A*, 380(25-26):2129–2135, June 2016.

[19] Le Bin Ho and Nobuyuki Imoto. Generalized modular-value-based scheme and its generalized modular value. *Phys. Rev. A*, 95(3), March 2017.

[20] Le Bin Ho and Nobuyuki Imoto. Various pointer states approaches to polar modular values. *J. of Math. Phys.*, 59(4), April 2018.

[21] A D Parks, S E Spence, and J M Farinholt. A note concerning the modular valued von neumann interaction operator. *uantum Stud. Math. Found.*, 6(1):101–105, May 2018.

[22] Kazuhisa Ogawa, Osamu Yasuhiko, Hirokazu Kobayashi, Toshihiro Nakanishi, and Akihisa Tomita. A framework for measuring weak values without weak interactions and its diagrammatic representation. *New J. Phys.*, 21(4):043013, April 2019.

[23] Xiaogang Li and Jiancun Tao. Measurement of modular values and connection to the annihilation operator. *EPL*, 131(5):50003, September 2020.

[24] Arun Kumar Pati. Super quantum search algorithm with weak value amplification and postselection. *arXiv preprint arXiv:1910.12390*, 2019.

[25] Elham Kashefi, Adrian Kent, Vlatko Vedral, and Konrad Banaszek. Comparison of quantum oracles. *Physical Review A*, 65(5):050304, 2002.

[26] Vikram Menon and Ayan Chattopadhyay. Quantum pattern matching oracle construction. *Pramana*, 95(1):1–3, 2021.

[27] Mirko Cormann, Mathilde Remy, Branko Kolaric, and Yves Caudano. Revealing geometric phases in modular and weak values with a quantum eraser. *Physical Review A*, 93(4):042124, 2016.

Neural Network-Enhanced Spectral Detection of Chromatin Loops

Michaël Liefsoens

Department of Mathematics, KU Leuven, Celestijnenlaan 200B, 3001, Leuven, Belgium
Department of Physics and Astronomy, KU Leuven, Celestijnenlaan 200D, 3001, Leuven, Belgium

To understand chromatin architecture and the functional role of that architecture, understanding loop formation has become crucial, as loops are involved in condensing chromosomes during mitosis; isolating structural domains; and allow interactions to occur between genes and their enhancers or inhibitors. Despite the emergence of increasingly powerful genome visualization techniques, the high variability in cell populations and the randomness of conformations still make loop detection a challenge. In this article, a recently published approach to tackle these issues is summarised and made less technical, giving intuition to the spectral and neural network methods used.

Introduction

Deoxyribonucleic acid, or DNA, is a huge molecule build of nucleotides (groups of a sugar, a base and a phosphate) that are bound together in specific base pairs to form a double helix structure. This double helix is wrapped around proteins called histones to make the DNA more compact in the cell. This DNA wrapped around the histones with a more-or-less constant genomic distance between the histones is called chromatin. All of this is taught in high school biology, and is standard knowledge by now. Historically speaking, however, we covered some of the research of the last two hundred years in biology. Now we know that sequences of specific nucleotides (distinguished via the bases) are responsible for the encoding of our genetic traits and that it is via DNA that our offspring is given some of our own genetic information. Imagine Darwin in 1859 with his *The origin of species* and his evolution theory, modelling that we pass on characteristics to offspring, with DNA only being discovered in 1869, see [7]. By 2003, all the genetic information encoded in human DNA (called the genome) was mapped and the Human Genome Project came to an end.

Even though we can all now look up the possible genes of our DNA, this information is far from the whole story. Take for example your hair, which may have some color variations, or even some gray hairs. Even though they are all hair cells, and all have the same DNA and the same DNA as a liver cell, the color is different. This is because not all the genes that are present are expressed equally in each cell. Epigenetics is the study of how behaviour and environment can cause changes in how your body reads DNA sequences. For example, if the sun is out and your skin gets more tanned, the environment is causing a change in the expression of the genes responsible for melatonin production. Another example is the (absence of) love of a parent that can cause reduced (or enhanced) stress reactions later in life, as evidenced in [9] for rat pups.

On a molecular level, what are the causes for the genes to be more or less expressed? One factor is the compaction of DNA: the tighter it is packed, the more difficult it is to read, and the less those genes are expressed. Another factor is the binding of molecules like methyl to DNA which form obstacles for the proper reading of the DNA, see [10] for an example of this in cells of smokers. A final factor we list is the presence of loops. Before every gene there is a *promoter* region, which intuitively is a road sign signalling that a gene is about to start, and that the copying process should start there. In [2], they show that the close spatial distance of another region on the DNA, called the enhancer, can stimulate the copying process. Intuitively, the enhancer is attracting the proteins so that they know where the promoter is and can start reading the DNA. They also showed that this enhancer can be very far away along the DNA, hence showing that the enhancer-promoter interaction is dependant of loops being formed on the DNA (to bring the enhancer close in spatial distance to the promoter).

By now, the loop extrusion mechanism is the standard model to explain how chromatin loops are formed. In this model, an SMC-protein (structural maintenance of chromatin) is bound to the DNA at some location, and then starts actively pulling the DNA on both sides to form a loop. This process continues until the right proteins are encountered that can bind the ends of the loop and the SMC-protein can detach. To experimentally follow this process, which is already being done, it is fundamental that the loop anchors are known in advance in order to measure their movements.

Clearly, loops are crucial for general compaction in the cell and for gene expression regulation via the enhancer-promoter interaction. Hence, detecting them is crucial as well. For this, most often Hi-C methods are employed. Intuitively, in these methods, the chromatin is immersed in glue and then cut into pieces. All these pieces are then examined, and if two pieces that are not next to each other are glued together, one knows that those parts of the chromatin were originally in close proximity. By repeating this process many times, a contact probability map is made, where a high probability of contact indicates the presence of a loop in the ensemble of chromatin. Unfortunately, this method destroys the chromatin in the process, and does not allow for a 3D reconstruction of the chromatin. Moreover, it averages over all the measurements, so loops that occur in a small part of the population may be averaged away. To overcome these difficulties, fluorescence in situ hybridisation, or FISH, has been developed. Also note that there are many more advanced techniques that are based on FISH, such as high resolution FISH and MERFISH. In these methods, fluorescent probes are bound to specific locations of the DNA and are monitored with microscopes. Skipping a lot of details, the method allows for a 3D-reconstruction of every single measured chromatin strand. Unfortunately, these outputs are most often analysed as if they were Hi-C measurements, by making an average distance map of all the measurements and interpreting this as a contact probability map.

Innovative methods are clearly needed to fully exploit this new data that FISH offers. In our work, we addressed the possibility of characterizing chromatin loops through an alternative approach based on the spectral representation of chain configurations, thereby leveraging the whole information of chain 3D spatial arrangement offered by sequential FISH methods. Additionally, we constructed neural networks (NN) to segregate looped and non-looped conformations at the single-cell level.

This paper is structured as follows. First, we give a way of modelling the intricate nature of chromatin in a much simpler way with polymer physics. Then, it is explained how Fourier analysis can help in understanding the different scales of the chromatin, and we construct a topological characteristic of looped polymers, called the log-spectral ratio Λ. Moreover, we explain how neural networks can help understanding the structure of the polymer, once the log-spectral ratio has pointed at a possible loop. The log-spectral ratio is applied to an experimental dataset, and the neural networks are also applied to obtain further insights in the local architecture of the chromatin.

Modelling DNA as correlated random walks

As we have seen in the previous section, DNA is quite complex to describe, being an enormous molecule. Even though we understand how DNA works on a more fundamental level—which base pairs with which base, and via which interactions–this is simply too much detail to work with to describe how DNA as a whole behaves in a cell (nucleus), both spatial configuration and its dynamics. For example, starting from the fundamental interactions of the hydrogen bonds and specific atoms, numerically simulating how a whole chromosome would behave in a cell nucleus simply takes too many resources. Therefore, we need coarse grained models to model and better understand DNA. Coarse grained models are a type of model that conserves (certain) macroscopic features, while ignoring microscopic details. The fundamental assumption behind this is that some macroscopic features are independent of atomic structure.

DNA is often modelled with coarse grained models in statistical physics. The idea is that many of DNA's properties come from the fact that it is a long chain with predominantly short-range interactions. The simplest model from this point of view, is the so-called Gaussian chain. In this simplest case, DNA is modelled as a simple polymer, i.e. a chain of beads with as only interactions the harmonic attraction between the two nearest neighbouring beads. Note that these beads can represent many things, in function of which scale we are interested in. For example, in a rather fine coarse grained model, we can treat each base pair as a bead. In other contexts, it might be better to model several thousands of base pairs as a single bead. As such, the polymer physics approach facilitates a general treatment of a bead-spring model, where the physical objects corresponding to a bead can be chosen according to the situation and the relevance of different scales. It is well-known–see for example [6]–that the configurations of these Gaussian chain polymers are just the result of following a random walk. Hence, to describe the spatial configuration of DNA at one time, we can generate a random walk.

As said earlier, the Gaussian chain is the simplest model for DNA configurations. To minimally, yet usefully, extend this model, we can consider correlated random walks. Imagine a very extended strand of DNA, then you can say that each bead of the polymer is positively correlated with the previous step. Indeed, to extend itself maximally, it would always walk in the same direction. On the other hand, to model a maximally compact strand of DNA, you would want to model the polymer as a negatively correlated random walk: a step in one direction has to be compensated with a step backwards.

To facilitate this modelling, we consider (sampled) fractional Brownian motion (fBm). This is a one parameter extension of a random walk, where the parameter $H \in [0,1]$–called the Hurst index–determines the degree of correlation of the random walk. As H tends to zero, the walk becomes perfectly negatively correlated, and for H going to unity, the walk becomes purely positively correlated. A random walk corresponds to $H = 1/2$. To describe such a correlated random walk of length N, consider the matrix Γ, whose entries are given by

$$\Gamma_{i,j} = \frac{i^{2H} + j^{2H} - |i-j|^{2H}}{2} \qquad 1 \leq i, j \leq N,$$

and define the symmetric matrix Σ as a matrix such that $\Sigma\Sigma = \Gamma$. Take N samples of white noise with variance σ_0^2, i.e. samples of a normal distribution with mean 0 and variance σ_0^2, and collect these samples in a vector $\vec{w}$. The correlated random walk $\vec{\gamma}$ is defined as $\vec{\gamma} = \Sigma\vec{w}$. One can check that the expected value of $\vec{\gamma}$ is zero, and that the covariance of γ_i and γ_j is given by $\sigma_0^2\Gamma_{ij}$. In particular, $\sqrt{\langle\gamma_n^2\rangle} = \sigma_0 n^H$, which agrees with our intuition: as H grows small, the walk will barely leave its initial point; and as H grows larger, the walk is expected to step further away.

Looped correlated random walks

To model looped DNA configurations, we consider looped correlated random walks. For this, we start from a correlated random walk, and bring the ends together to form a loop. Mathematically, following [1], this corresponds to changing the process $\vec{\gamma}$ to the process $\vec{\lambda}$ as

$$\lambda_n = \gamma_n - \mathcal{B}_H(n; 0, N)V, \tag{1}$$

where $V = \gamma_N - \gamma_1$ is the end-to-end vector and the bridge function $\mathcal{B}$ is given by

$$\mathcal{B}_H(n; 0, N) = \frac{1}{N^{2H}}\Gamma_{n,N}.$$

The process $\vec{\lambda}$ is what we will use to model looped DNA strands.

Fourier analysis on polymers

To detect loops in polymers, we predominantly need to consider the large-scale features of the polymer, and not the smallest scales. In a sense, we have to many information in the exact positions of the polymer: we only need to know if two beads that are far along the chain are close in spatial distance. All the positions and interactions of the beads in between matter much less. This fact also makes it possible to model DNA as a correlated random walk, as the smallest scale interactions do barely matter for detecting loops in static configurations.

When we want to separate different scales in a problem, Fourier analysis is often a great help. Also for polymers, this is the case. In [4], a tool is described to perform a Fourier-like transform on a polymer and to separate the different scales at play. We will shortly recall this transform of the polymer, its benefits, and–in the next section—how it helps to detect loops.

The global idea is as follows. Given a polymer configuration $\vec{x}$ of N 3D-coordinates, we can consider the three length N signals x_n, y_n and z_n. For each of these signals x_n, we take the discrete cosine transform (DCT, see later) to obtain $\mathrm{DCT}_x(p)$. By squaring this number and adding them up for each p separately, we get the power spectral density (PSD) $\widehat{\mathcal{E}}$ as

$$\widehat{\mathcal{E}}_p(\vec{x}) = \mathrm{DCT}_x(p)^2 + \mathrm{DCT}_y(p)^2 + \mathrm{DCT}_z(p)^2.$$

This number represents the distribution of the total energy over the different modes of the DCT. The average of this power spectral density is what we will use in the remainder of this work.

Finally, we discuss the DCT in a bit more detail. Given a 1D-signal x_n with $n \in \{0, \ldots, N-1\}$, we find the DCT as

$$\mathrm{DCT}_x(p) = \frac{1}{N} \sum_{n=0}^{N-1} x_n \cos\left(\frac{p\pi}{2N}(2n+1)\right).$$

This can be computed efficiently as there is a close link to the fast fourier transform (FFT) for numerical signals. We call $\mathrm{DCT}_x(p)$ the pth mode of x. Intuitively, for low p, the pth mode gives information of the largest scales. As p increases, the mode starts giving information on the small scale behaviour of the signal. Concretely, it can be shown that X_0 is just the average of the signal, or the centre of mass. The first mode is intimately related to the end-to-end distance of the signal: its absolute value corresponds roughly to $|x_{N-1} - x_0|/N$. Similarly, the higher order modes can be understood as follows. The pth mode gives information of the average extent of length N/p sub-polymers. By taking the power spectral density of the three coordinate signals, we obtain a result that is less dependent on the exact position and orientation in space, and the average of these numbers is non-zero.

To guide your intuition, you may think of the PSD as actually detailing how the total energy is distributed over all the scales. For example, for random points in space, the PSD is for all modes the same on average: every scale gets equal parts of the energy, as there is no structure within the point cloud, and the randomness makes it scale-invariant. On the other hand, for a random walk (which may model a polymer), the points cannot jump too far in each step, and so there is structure within the resulting point cloud. An example of an averaged PSD for a random walk is shown in Figure 1 (blue curve). Clearly, there is much less energy for the high modes (small length scales) than for the low modes (large length scales). Think of it as follows, even with blurry glasses, such that the exact positions of the beads become invisible, the general shape of the walk in space is still visible: for a polymer, there is much more energy stored in the larger scales than in the exact details at the small scales.

Log-spectral ratio Λ and Λ-plot

As detailed in the previous section, the PSD for a polymer has a certain structure, as the short scale behaviour is much less important for the global shape. In [4], it is shown that by taking the slope of the line connecting the first and second mode in a log-log plot, you can determine if the polymer is in a condensed or extended state. (Indeed, it is only the largest scales that are needed to determine the folding state.) Looking at the PSD for a looped and non-looped random walk in Figure 1, we can make similar observations about the lowest modes. One can observe that the odd modes are lowered for the looped random walk, while the even ones remain unchanged. This can be shown analytically, and is even of topological nature, i.e. the underlying process does not matter. For details on the proof of this statement, see [5]. The key intuition for this fact is that the endpoints must come close for a loop, and thus the odd modes

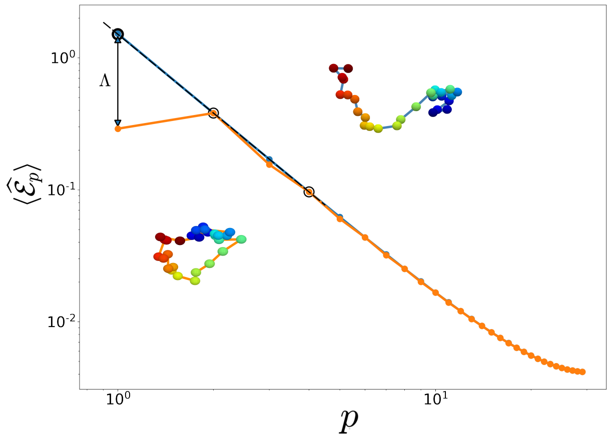

Figure 1: *Theoretical PSD for a random walk (blue curve) and the corresponding looped random walk (orange curve). Snapshots show one specific conformation before (upper) and after (lower) looping by means of Equation Equation (1). The parameter $\Lambda(x)$ is the difference between the observed first mode (here for the looped conformations) and the expected first mode extrapolated from the second and fourth modes (see black dotted line and circles). Figure is taken from [5].*

(which make the endpoints disconnect) cannot be too large. Since the even modes are expected to remain unchanged, we can probe the power law behaviour of the polymer from the second $\langle \widehat{\mathcal{E}}_2 \rangle$ and fourth $\langle \widehat{\mathcal{E}}_4 \rangle$ modes. Extrapolating from this power law, we obtain an estimate for the first mode $\langle \widehat{\mathcal{E}}_1 \rangle$. Comparing this estimate with the actual first mode gives the log-spectral ratio Λ, see Figure 1. In formulae,

$$\Lambda = \log\left(\frac{\langle \widehat{\mathcal{E}}_2 \rangle^2}{\langle \widehat{\mathcal{E}}_1 \rangle \langle \widehat{\mathcal{E}}_4 \rangle}\right). \tag{2}$$

With this definition, the log-spectral ratio exactly measures the difference between what is expected from a non-looped polymer and what is observed for that polymer. If that difference is too high, it means the largest scale is much smaller than expected, signalling that the polymer has a loop.

Computing the log-spectral ratio for a random walk analytically, we find $\mathcal{O}(N^{-2})$ and $\log\left(\frac{\pi^2}{\pi^2-8}\right) + \mathcal{O}(N^{-2}) \approx 1.66 + \mathcal{O}(N^{-2})$ for looped random walks. Clearly, this observable discerns looped and non-looped random walks. Performing simulations, we could show that this observable remains reliable to differentiate looped and non-looped polymers, even if different degrees of correlations or even self-interactions are added. For details, see [5].

In experimental data of human DNA, of course, we are not looking for isolated DNA loops. Instead, we are looking for inner loops in large DNA strands. For this, we want to consider all sub-polymers at once and compute the log-spectral ratio of each of them. To this end, we introduce the following coordinates on the polymer. Given a sub-polymer from bead i until bead j, we denote the midpoint $\iota = (i+j)/2$ and the length $\eta = |i-j|$. The coordinates (ι, η) then represent the sub-polymer from bead $\iota - \eta/2$ to bead $\iota + \eta/2$. Computing the log-spectral ratio Λ for each of these sub-polymers, and putting it together in one heat map, we get the Λ-plot, as visualised in Figure 2 for an example.

As is evident in Figure 2, the maximum in the Λ-plot does not exactly represent the looped sub-polymer. Doing analytical computations for (looped) random walks and verifying with multiple simulations, a link is established between the maximum of the Λ-plot and the exact position of the loop. The key here is: find a maximum, you find a loop.

We now have the following algorithm to detect loops in an ensemble of polymers with inner loops. First, make the Λ-plot. Second, find all maxima (ι, η). There is a constant $\mu_0 \approx 1.34767$ so that the estimated loop falls between monomers $\iota - \eta/(2\mu_0)$ and $\iota + \eta/(2\mu_0)$.

An important remark needs to be made. A more intuitive approach to loop detection would be to consider the distances between any two beads and look for low values (with respect to some threshold) in those distances. However, the very measuring technique of multiplexed FISH data does not allow this on this resolution. Indeed, the coordinates obtained are very precise, but are fitted with a Gaussian to fluorescent spots of strands of DNA. In our polymer model, this corresponds to taking a high resolution polymer with an inner loop, and then taking the centre of mass of consecutive fixed length sub-polymers. These centres of mass then form the coordinates that we have access to. There is no guarantee that the presence of a loop, and the consequent dip in monomer-monomer distance, is still visible in the coarser polymer. Even stronger, we showed in [5] that this distortion will occur in simulated data and that simply looking at the distances is no longer a dependable indicator of loops. The spectral approach overcomes this difficulty better by looking on the global features of

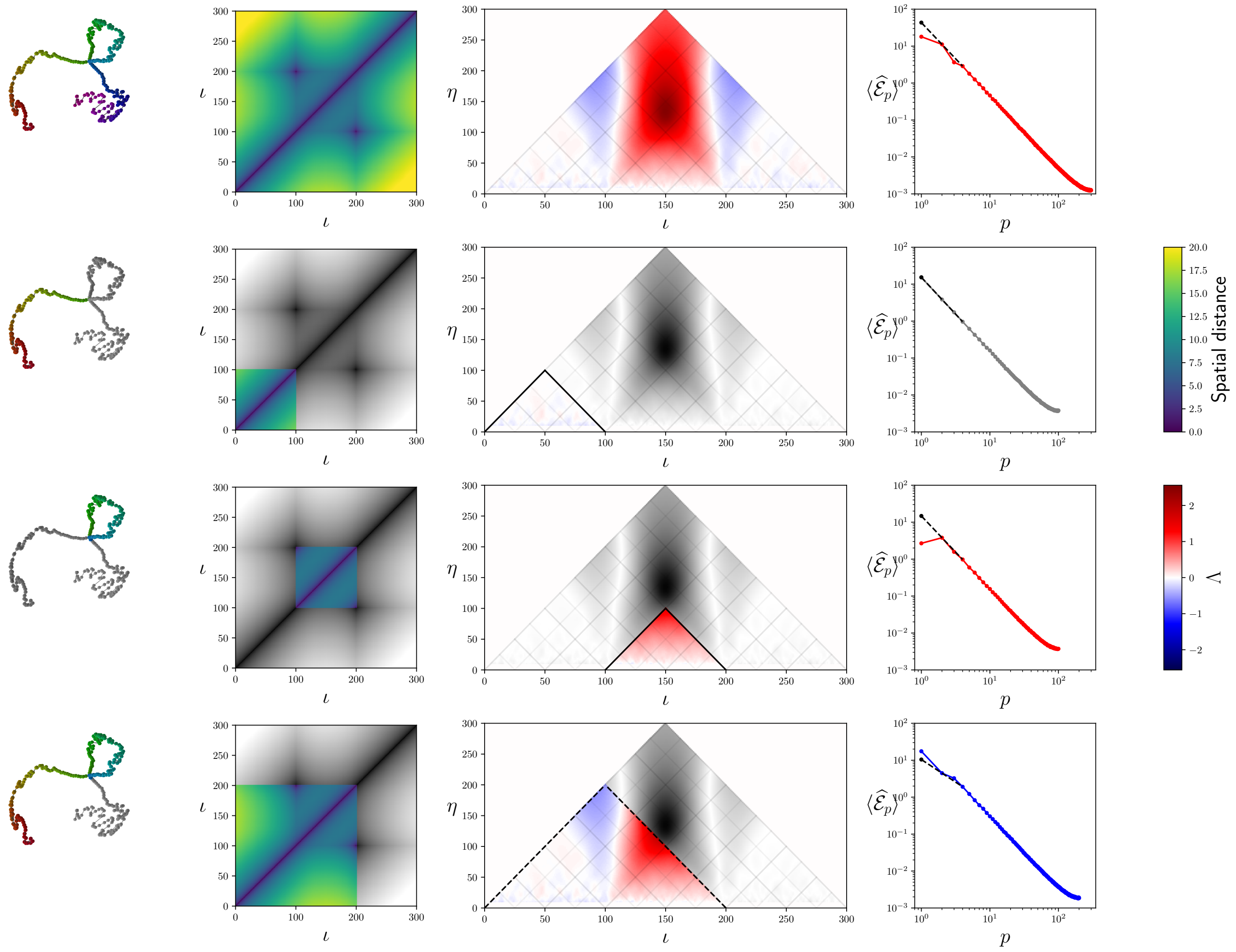

Figure 2: *Λ-plot example for an ensemble of 2000 samples of a (random walk) polymer with N = 300 monomers, all containing an internal loop of size 100 in the middle. Different rows focus on distinct sub-regions of the same polymer: whole polymer; first third; inner loop; first two thirds (including the loop). The first column displays a mean polymer configuration (for details, see [5]). The second column shows the distance map of the polymer, while the third column shows the Λ-plots. The regions selected in each row are highlighted in every column. The spectrum for the selected sub-region is shown in column 4. Figure taken from [5].*

bending and loop formation, which most often still shows after the experimental coarse graining.

Application to experimental data

To assess the performance of the Λ-plot method on experimental data, we first applied it to selected regions of mouse embryonic stem cells, for which Hi-C and FISH measurements are available. Our method was able to detect most of the loops identified with other methods, and to detect previously non-detected loops. This is due to the fact that it analyses the entire conformation between two loci, instead of a simple evaluation of the end-to-end distance. From this benchmark, we also noted that our method is prone to localization errors in regions with complex architectures, where, for example, several loops are nested. Then, the presence of the loops is detected, but their position or size is less accurate.

Next, we applied our method to the experimental data of [3]. There are two datasets available: one wild-type (unaltered) dataset and one measurement set that has been treated with Auxin, in order to remove the proteins (CTCF) ought responsible to keep loops in place. From the distance maps and Hi-C contact maps in Figure 3, it is immediately clear that a lot of structure has indeed been lost after treatment with Auxin. However, in [3] it is argued that one the single-cell level many structures are still present, but that their preferential sites simply no longer agree. This turns out to be the effect of CTCF: to give preferential positions of loops. This finding is consistent with our analysis, as the Λ-plots in Figure 3 immediately show a lot of structure in both datasets. Note that almost all loops predicted by the Λ-plot are invisible on the Hi-C and distance maps. This is expected to be an averaging effect, to which the Hi-C and distance plots are more sensitive than the Λ-plot. Specifically, we detect 14 loops (labelled 1-14) in the wild-type (WT) data and 8 loops (labelled A1-A8) in the auxin-treated variant. Notice how in the wild-type cells, loop extremities align with regions rich in the RAD21 protein, which implies that they are likely due to cohesin-mediated loop extrusion halting at a physical barrier, likely CTCF. For the Auxin treated cells, we also gave other options in [5] for the origin of these loops.

Neural networks

To further validate our approach and also extend it as to give information for single cells, we use neural networks. In principle it is possible to just look through every possible sub-polymer and see if it is a loop or not, but in practice this takes to much computing time and energy. Instead, we use the Λ-plot to pinpoint possible locations in the ensemble where statistically significant loops are present, and then investigate those regions for every measurement with a neural network.

For each possible loop location, we train a neural network on (looped) random walk data of the same size, and then apply it to the experimental data. The output is the probability of the sub-polymer to be looped or not. We decided that a probability of 50 percent or higher indicates a present loop, and otherwise we call it non-looped. It is important to note that the fact that we can use artificial data to train the neural networks is a significant advantage. Indeed, otherwise we would have to waste valuable experimental data and still have less training data than now.

Finally, we note that the measurement technique (of fitting with a Gaussian to fluorescent spots) necessitates that the neural network training data followed the same kind of procedure. For this, we take high resolution walks, and coarse grain them by taking the centre of mass of consecutive equal-length sub-polymers. Thanks to this, the neural networks learns to recognise more global features of the loops, instead of the typical close contact of two points. In Figure 4, we see an example of the output of the neural network segregation for loop A4.

Insights into local chromatin architecture

Because we can detect loops and also segregate the measurements with and without a specific loop, we can also consider the effect of the loops on previous analyses done. For example, scaling laws of genomic distance that previously pointed to a specific model (the crumpled globule), change drastically when the looped and non-looped measurements are analysed separately. Instead, they point to another model where multiple exponents are possible, and which also allows the cell to activate and deactivate DNA as needed. For details, we point to [5]. Furthermore, thanks to the neural network segregation, we can also consider correlations between loops formed, and see interesting things there as well. Many more questions can now be asked and investigated due to this new method, and we refer to [5] once more. In summary, this method helps gain more understanding of the local chromatin architecture.

Discussion

Despite their high accuracy in determining the three-dimensional structure of chromosomes, multiplexed FISH experiments can only visualize the centre of mass of probe segments. The detection of loops in this type of data hence becomes quite challenging. Indeed, our study on synthetic data confirmed that this limited resolution masks the presence of multiple loops. Yet, FISH experimental data offers more comprehensive information than distance maps by encompassing the complete 3D configuration, information that has been overlooked until now.

Using all the 3D information, the Λ-plot provides a reliable and fast method to detect loops in synthetic as well as experimental multiplexed FISH data, irrelevant of size and position, and sensitive to small looped populations. The method takes great advantage of the large-scale characteristics of (looped) polymers, and is therefore more robust to detect loops in a chain than small-scale properties

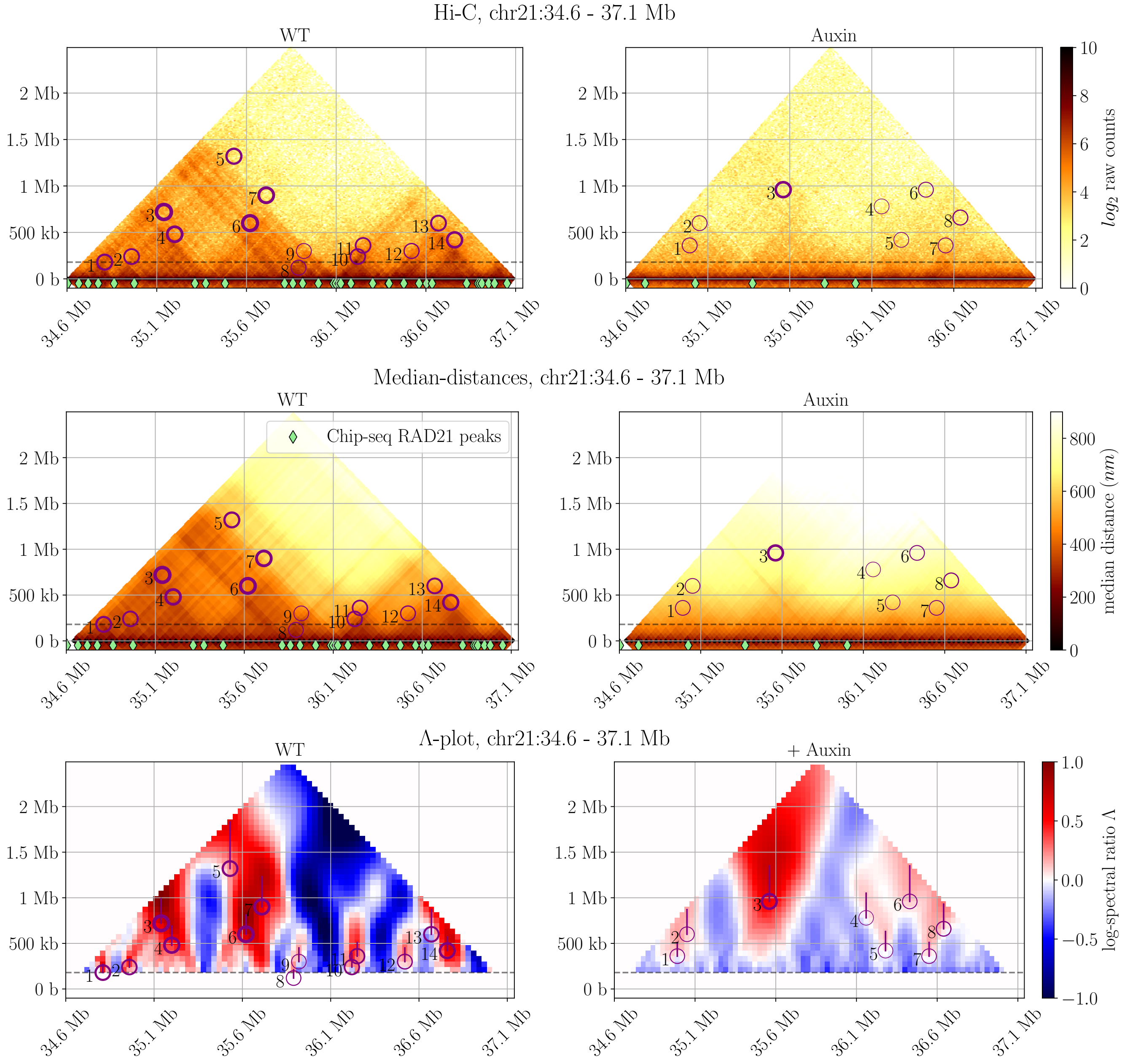

Figure 3: *The Λ-plots (a), distance maps (b), and Hi-C maps (c) for the experimental data of Bintu et al. for both the wild-type variant (left) and an auxin-treated variant (right). The coordinates along the chromatin are the same for each plot, making direct comparisons of positions possible. A given point within a plot corresponds to the interaction between two points along the chromatin. For example, the tip of the triangle gives information about the interaction between the first and last point. By moving along the left edge of the triangle to the bottom, you consider the interaction between the first point and points closer and closer to the first point. a) Purple lines link the positions of Λ maxima and detected loops. In each plot, purple circles indicate the location of loops detected by the Λ-plot procedure. The symbol linewidth is proportional to the corresponding maximum Λ intensity. Each detected maximum is given a loop id. On the bottom of the distance and Hi-C plots, green diamonds represent the presence of the Rad21 protein. Figure taken from [5].*

that are sensitive to fluctuations and measurement errors.

Using neural networks, the presence of loops is confirmed, and allows to segregate cells based on the presence of specific loops. This process is fast and reliable, where the latter is partly attributed to the initial guidance provided by the Λ-plot, which also provides a physically interpretable and mathematically sound basis for the detection pipeline. Thanks to the ease with which we can generate artificial training data based on an fBm model, we can furthermore

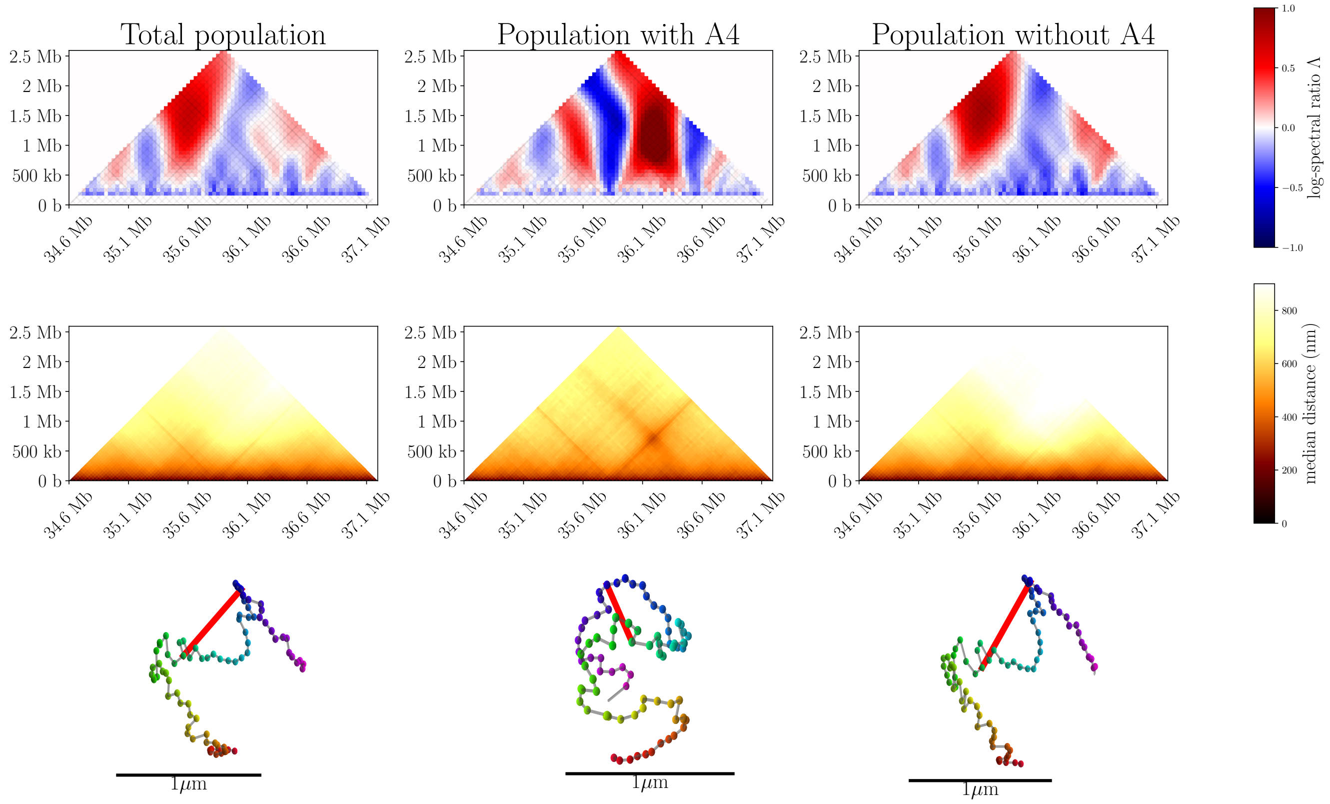

Figure 4: *Typical example of output of neural network segregation of looped and non-looped populations. We focus on loop A4 (detected in 24 % of the population). The first column shows the Λ-plot, distance map, and mean configuration for all measurement data. The second and third columns show Λ-plot, distance map, and mean configuration for measurements that the NN recognized as containing or lacking loop A4, respectively. The end-to-end distance (length of the red segment) in the mean configuration is 640 nm, 547 nm, and 710 nm,respectively. Notice how the presence of the loop A4 results in a high maximum in the Λ-plot, and a dip in the average distance in the distance-plot (second row). Moreover, in the third column, the absence of loop A4 makes the corresponding maximum of the Λ-plot disappear, and the average distances there larger. Notice in the mean configuration (third row) how the end-to-end distance between the predicted loop anchors is much smaller when loop A4 is predicted to be present. Figure taken from [5].*

avoid wasting valuable measurements. Our approach outperforms distance-based approaches on loops already detected through Hi-C maps as demonstrated in [5] for the benchmarking data.

For other experimental data, where previous analysis was unavailable, and where both wild-type and cohesin-depleted measurements were available, we detected loops in both datasets with comparable occurrence frequencies, in different locations. Strong correlations of the locations of loops with biological markers (such as Rad21) were found, even though determining completely the biological determinants at the origin of these loops is beyond the scope of this work.

The ability to examine loops at the single-cell level allows to answer new questions regarding the structure of chromatin. By, for example, for the first time considering the correlations between loops, we can get more understanding of the potential existence of clusters of adjacent loops that result in a flower-like structure. Moreover, we evidenced the frequent presence of correlation between loops that are nested one in the other and sharing one end. This rather unexpected finding surely deserves to be further investigated on alternative datasets.

The method introduced here broadens data processing possibilities and strengthens the foundation for advancing chromatin's theoretical understanding through precise and comprehensive experimental data analysis. We discovered that the corresponding critical exponents of 1/3, frequently encountered in experimental data, may result from averaging looped and non-looped configurations within a dataset. This effect may have remained unnoticed due to the need for a prior looped conformations segregation.

Multiple future research endeavors are possible with the developed method, and we highlight one topic that warrant further exploration. The versatility of the spectral-based technique developed in this study could be applied to investigate a broader range of phenomena. For instance, the method can be adapted for detecting plectonemes in supercoiled DNA or for identifying density variations across the genome or in spatial arrangements, such as alternating coils and globules, or alternating A and B compartments. These structures are predominantly characterized by their large-scale behaviors, where low-mode spectral features prove to be particularly suitable for in-depth investigation. Preliminary investigations of data from [8], which is on a much larger scale than the one considered here, seems to indicate indeed that the same analysis can readily identify AB-compartments and their corresponding boundaries. These findings are consistent with the conclusions drawn in the original paper. Additionally, loops were also detected and warrant further investigation in future research.

Acknowledgements

The content in this article is based on the author's master's thesis and the corresponding article [5]. The author likes to acknowledge the collaboration with Barbi M. and Földes T. and their guidance during his master's thesis, partially at Sorbonne University (Paris). In the same context, he would like to thank Carlon E. for bringing us in contact, and his support. Finally, I thank the Belgian Physical Society for their recognition of this work, and for the price for my master's thesis. Michaël Liefsoens is supported by the Research Foundation Flanders (FWO) with project 11PG324N.

References

[1] Abel symposia. *Stochastic Analysis and Applications: The Abel Symposium 2005. Proceedings of the Second Abel Symposium*. Springer e-books, Berlin (2007).

[2] Banerji, J., Rusconi, S. and Schaffner, W. *Expression of a β-Globin Gene Is Enhanced by Remote SV40 DNA Sequences*. Cell (1981).

[3] Bintu, B. and Mateo, L. J., Su, J. et al. *Super-Resolution Chromatin Tracing Reveals Domains and Cooperative Interactions in Single Cells*. Science (2018).

[4] Földes, T., Lesage, A. and Barbi, M. *Assessing the Polymer Coil-Globule State from the Very First Spectral Modes*. Physical Review Letters 127, 277801 (2021).

[5] Liefsoens, M., Földes, T. and Barbi, M. *Spectral-based detection of chromatin loops in multiplexed super-resolution FISH data*. Nature Communications 15, 7670 (2024).

[6] Mark, James E. *Physical Properties of Polymers Handbook* (2nd edition). Springer, New York (2006).

[7] Pray, L. A. *Discovery of DNA Structure and Function: Watson and Crick*. Nature Education (2008).

[8] Su, J., Zheng, P., Kinrot, S. S., Bintu, B. and Zhuang, X. *Genome-Scale Imaging of the 3D Organization and Transcriptional Activity of Chromatin*. Cell (2020)

[9] Szyf, M., McGowan, P. and Meaney, M. J. *The Social Environment and the Epigenome*. Environmental and Molecular Mutagenesis (2008).

[10] Zong, D., Liu, X., Li, J., Ouyang, R. and Chen, P. *The Role of Cigarette Smoke-Induced Epigenetic Alterations in Inflammation*. Epigenetics & Chromatin (2019).

Deciphering atmospheric escape to model oxygen loss from Earth

Maria Luisa Alonso Tagle[1,2],
Romain Maggiolo[1], **and Johan De Keyser**[1,2]

[1] Royal Belgian Institute for Space Aeronomy, Brussels
[2] Centre for mathematical Plasma-Astrophysics, KU Leuven, Leuven

Atmospheric escape plays a significant role in the long-term evolution of planetary atmospheres, and therefore in the development and sustainability of habitable conditions. In this work, we investigate the evolution of the atmospheric oxygen escape on Earth from current data towards the Great Oxidation Event (GOE), 2.45 billion years ago. We develop a semi-empirical model tracking seven different escape mechanisms that takes into account the past variations of the solar and planetary conditions until the GOE, allowing us to estimate oxygen escape rates in the past. Our analysis reveals a substantial increase in the total oxygen escape rate towards the GOE. This has led to a reduction of over 60% in Earth's oxygen content during the last 2.45 billion years, primarily attributed to polar processes. We highlight the importance of integrating multiple escape mechanisms to estimate atmospheric escape and identify key parameters that need to be taken into account when evaluating long-term atmospheric presence.

Introduction

As we venture into the discovery of rocky exoplanets, the need to refine the definition of habitability increases. Currently, the habitable zone is defined as the region around a star within which liquid water can be stable on a planet's surface. This distance-based approach overlooks the ability of a planet to retain water over the long term. Indeed, planetary parameters, like the composition of its atmosphere or its magnetisation –both mostly independent of the distance to the star– affect the capacity of the planet to retain water and maintain an atmosphere. Therefore, to understand the long-term habitability of a planet, it is crucial to examine the processes that drive atmospheric loss, leading to changes in the atmospheric composition. The escape of atmospheric particles can be driven by multiple energy sources. In the solar system, on the one hand, solar radiation plays a significant role by heating up and ionising the atmosphere. On the other hand, the complex interactions between the solar wind and the planet can also heat and accelerate atmospheric material [Gronoff et al. 2020].

The solar wind is the plasma outflow ejected by the solar corona at supersonic speeds (see transparent yellow lines in Figure 1). Near Earth, this plasma encounters the magnetosphere (see transparent blue lines in Figure 1), which is a region in space that is dominated by the Earth's intrinsic magnetic field. The magnetopause, the outer boundary of the magnetosphere, deflects the incoming solar wind. When the planetary magnetic field is strong enough, as with Earth, a large-scale intrinsic magnetosphere surrounds the planet and protects the atmosphere from direct solar wind interaction. For planets with weak or absent intrinsic magnetic fields, such as Mars and Venus, interactions between the solar wind and the planet's upper atmosphere generate electric currents that form an induced magnetosphere. Such planets are considered unmagnetised.

A longstanding hypothesis suggests that a planetary magnetic field shields the atmosphere from escape by deflecting the solar wind [Lundin et al. 2007]. However, spacecraft observations at Earth, Venus, and Mars reveal that the current atmospheric escape rate on Earth is comparable to or even exceeds that of its unmagnetised neighbouring planets, challenging this statement (see [Ramstad & Barabash 2021] and references therein). In this light, [Gunell et al. 2018] explored the role of the planetary magnetic field in atmospheric escape for terrestrial planets, using a semi-empirical model. Following a similar approach, we examine how past planetary and solar conditions have influenced oxygen escape rates over geological timescales, until the Great Oxidation Event (GOE), which is a step increase in the concentrations of molecular oxygen in the atmosphere, caused by the emergence of life.

There are two main physical limits that will determine whether an atmospheric particle will escape or not: an energy limit and a supply limit [Ramstad & Barabash 2021]. The energy limit is given by the amount of energy transferred to atmospheric particles, as more energy transferred to the particles facilitates their escape. The supply limit is reached when there are no more particles available to escape, thus the limit is the ion supply from the ionised upper atmosphere, also called the ionosphere.

The exobase is the atmospheric boundary above which particle collisions become negligible. Below this boundary, collisions dominate and particles are thermalized, the bulk flow energy is quickly converted into thermal energy. Above it, any energization process can increase the velocity of particles allowing them to escape. For this reason, we define the exobase as the lower boundary in our model, as it represents the transition point where escape processes become significant.

Method

Our goal is to calculate the oxygen escape rate from Earth in the past in order to estimate the total atmospheric oxygen loss into space, and to understand key aspects of atmospheric escape.
Two factors influence atmospheric escape: solar forcing and planetary conditions, both of which have changed over time. On the one hand, the young Sun had a denser and faster solar wind [Carolan et al. 2019], and emitted more intense Extreme UltraViolet (EUV) radiation [Ribas et al. 2005], therefore promoting atmospheric oxygen escape. On the other hand, the Earth's magnetic field [Bono et al. 2022] and exosphere also changed over time, further complicating the long-term evolution of oxygen loss.
We explore seven different escape mechanisms and how they change with the evolution of the Sun and the Earth. When an analytical approach is not possible, a semi-empirical model is used: observed escape rates are scaled depending on the coupling between the evolving Sun and evolving planetary environment, and on the area or volume of the region where the oxygen escape takes place.
We account for the ionospheric supply by limiting the escape flux to a maximum flux depending on the solar EUV radiation [Barakat et al. 1987].

Magnetic Field Model

We use a magnetic field model to estimate the area or volume of the oxygen ion escape regions and to determine the magnetospheric cross-section with the solar wind.

Magnetopause Standoff Distance

The magnetopause standoff distance is the shortest geocentric distance to the magnetopause (in Figure 1: r_{MP}). It is calculated as the balance point between the solar wind dynamic pressure and the magnetospheric magnetic pressure. When the solar wind pressure increases or the planetary magnetic moment decreases, this distance is reduced.

Magnetospheric Cross-section

The magnetic field model provides the magnetospheric cross-section with the solar wind

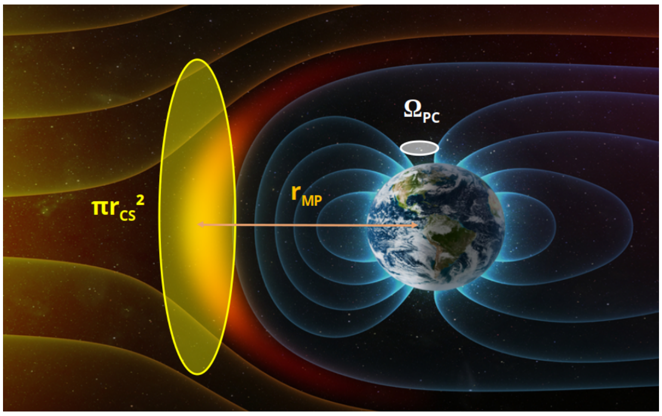

Figure 1: *: Illustration of our magnetic model. The magnetopause standoff distance is r_{MP}, the magnetospheric cross-section is πr_{CS}^2, and the solid angle of the polar cap is Ω_{PC}.*

(in Figure 1: πr_{CS}^2). As the solar wind pressure increases or the planetary magnetic moment decreases, the magnetospheric cross-section is reduced.

Solid Angle of the Polar Cap

The solid angle enclosed by the Earth's magnetic field lines that connect the upper atmosphere to the solar wind defines the extent of the magnetic polar cap (in Figure 1: Ω_{PC}). These open magnetic field lines represent a preferential escape path for atmospheric particles. The solid angle of the polar cap expands with increasing solar wind pressure or decreasing planetary magnetic moment, enhancing the potential for atmospheric escape.

Escape Mechanisms

Our model considers the seven main atmospheric escape processes observed in terrestrial planets in our Solar System [Gunell et al. 2018]: Jeans escape, photochemical recombination, ion pickup, sputtering, cross-field ion loss, polar wind, and cusp escape.

Thermal escape mechanisms

Thermal escape mechanisms depend on the upper atmospheric temperature, as higher atmospheric temperatures imply higher particle velocity, increasing the escape rate. Given the low atmospheric temperature of the Earth, only one mechanism is at play.

Jeans escape This mechanism refers to neutral particles at the tail of the velocity distribution, which have higher velocities than the escape velocity, and do not collide with other particles. For Earth it has a minor contribution, nonetheless it is considered in our results.

Escape mechanisms in the unmagnetised regime

The following three mechanisms are relevant for unmagnetised planets, like Mars or Venus, but they are negligible for Earth.

Photochemical Recombination Solar wind electrons recombine with planetary oxygen ions, creating an energetic oxygen atom. However, the kinetic energy of the resulting oxygen atoms remains well below their gravitational binding energy, preventing them from reaching the escape velocity and their contribution to oxygen escape is zero.

Ion Pickup Planetary neutrals that are ionised by solar wind charge exchange, electron impact, or by solar EUV, can be picked up and accelerated by the solar wind magnetic field and ejected from the atmosphere. Their escape rate depends on the amount of gravitationally bound neutrals outside the magnetosphere, which for Earth is negligible over the time period considered in this study.

Sputtering Ions accelerated by the solar wind collide with planetary neutrals transferring them energy, which may be sufficient to let them escape. The corresponding escape rate depends on the amount of gravitationally bound neutrals outside and slightly inside the magnetopause, which is negligible on Earth. Sputtering also happens inside the magnetosphere in the auroral zones, where it has a minor contribution that is included in our model.

Escape mechanisms in the magnetised regime

These mechanisms are relevant for magnetised planets, like Earth.

Cross-Field ion loss Ions initially trapped by the Earth's magnetic field on closed magnetic field lines (with both ends connected to the Earth) can escape across the magnetic field lines through plasmaspheric wind and plasmaspheric plumes. In our model, the corresponding escape rate depends on the exobase surface area outside the polar cap. It is a highly variable and complex escape process.

Polar Wind Ions escape along the open field lines of the polar cap, driven by the ambipolar electric field. This ambipolar field arises to maintain charge neutrality, as ionospheric electrons attempt to escape to space, driven by thermal pressure, pulling ions along with them. The escape rate depends on the polar cap area at the exobase altitude as well as on the temperature and density of ions and electrons in the ionosphere.

Cusp escape The cusp is a region in the polar cap where solar wind has direct access to the upper atmosphere allowing it to transfer part of its kinetic energy. This energy contributes to the heating and acceleration of ionospheric particles leading to their subsequent escape. The corresponding escape rate depends on the cusp area at the exobase altitude, the solar energy flux, and the magnetospheric cross-section with the solar wind.

A key challenge in estimating cusp escape is to determine the current cusp area at the exobase altitude, which is not well determined. As mentioned by [Nilsson 2011], knowing the correct area to integrate the cusp escape flux is critical to determine the total cusp escape rate. Therefore we studied different cusp areas at the exobase altitude, as smaller cusp areas will give smaller cusp escape rates.

We also used a higher ionospheric supply for cusp escape than for polar wind. The cusp is a region where solar wind particles precipitate in the atmosphere, which increases the atmospheric ionisation, and thus the maximum escape flux at the cusp [Schillings et al. 2018].

Results and Analysis

Past solar and planetary conditions

Figure 2 shows the evolution of the solar wind pressure and the solar EUV radiation towards the GOE, 2.45 billion years ago, with their current average values observed by satellites. The solar wind pressure increases by more than one order of magnitude towards the past. We use a solar wind model that gives the velocity and density of the solar wind over time, allowing to calculate how the solar wind affects each non-thermal escape mechanism. Meanwhile the $F_{10.7}$ index, which is related to the solar EUV radiation flux, increases exponentially, more than doubling its current value. The primary effect of the solar EUV radiation is heating up Earth's atmosphere (as shown in the bottom part of Figure 3), and the ionisation of neutral particles, thus increasing the ionospheric supply.

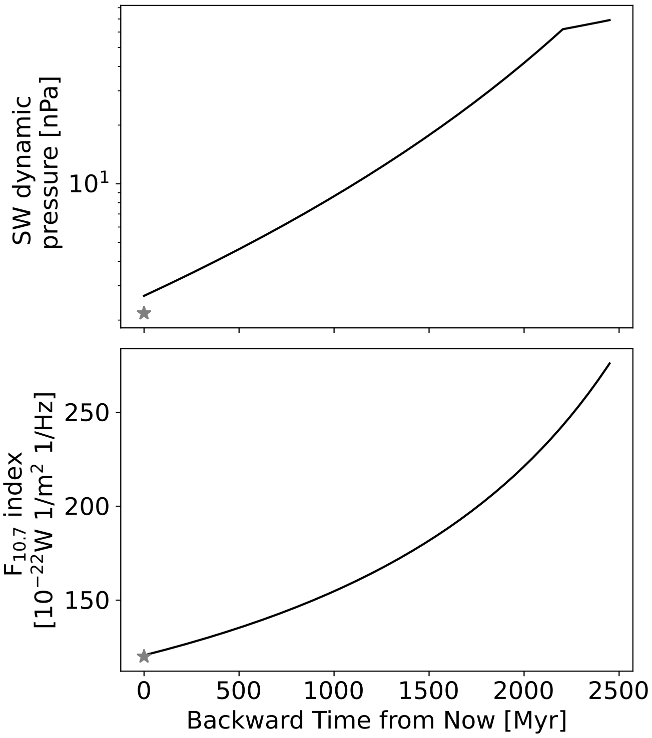

Figure 2: *Evolution of the solar parameters. Top panel: solar wind model by [Carolan et al. 2019]. Bottom: solar EUV flux model by [Ribas et al. 2005] converted to the historical $F_{10.7}$ index. Grey stars represent current average values observed (OMNI database).*

Figure 3 shows the evolution of the Earth's magnetic moment and of the oxygen temperature at the exobase altitude. The intensity of the Earth's magnetic dipole fluctuates over time, but it remains in the same order of magnitude. Together with the solar wind, it controls the magnetospheric geometry. The temperature at the exobase altitude increases towards the past, following the solar EUV radiation. This leads to a slight expansion of the exosphere,

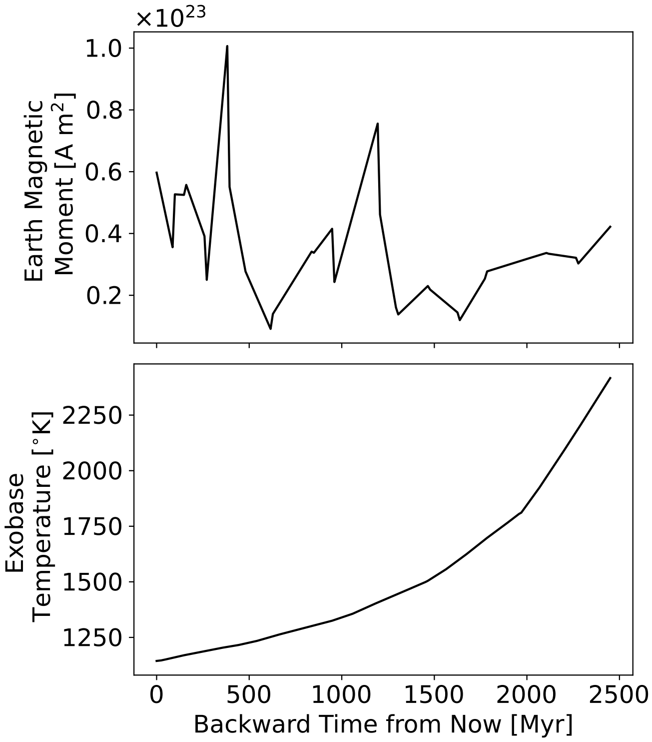

Figure 3: *Evolution of the planetary parameters. Top panel: Earth magnetic moment by paleomagnetic data ([Bono et al. 2022]). Bottom: Exospheric model depending solar EUV flux ([Johnstone et al. 2018]).*

which increases the exobase surface.

Oxygen escape

The primary findings of this study are represented in Figure 4. The solid red line represents the total oxygen (neutral and ion) escape rate, summing contributions from all seven escape mechanisms in our model. The dashed blue curve indicates the polar wind oxygen escape rate, the dotted green curve shows the cusp escape rate for the maximum cusp size considered in our model (with a magnetic latitudinal and longitudinal extent of 8° and 90°, respectively), and the dashdotted cyan line corresponds to the cross-field ion loss. Our results reveal that the two primary contributors to the oxygen escape from Earth are polar wind and cusp escape. While cusp escape is the dominant mechanism at present, our model suggests that in the past, polar wind was the leading contributor to oxygen loss.

The polar wind escape rate increases as solar wind pressure rises, driven by two combined effects: on the one side the oxygen escape flux increases due to stronger solar forcing, and on the other side, the polar cap expands. Meanwhile, the Earth's magnetic moment affects the polar cap size, introducing fluctuations in the escape rate. As the Earth's magnetic moment increases, the polar cap shrinks leading to a reduction in the total escape rate. A higher solar EUV flux increases the oxygen escape flux, and it increases the value of the maximum oxygen flux that can be extracted from the ionosphere. The increasing ionospheric supply is observed before 1500 Myr. ago (see Figure 4), when the oxygen escape through polar wind reaches saturation, meaning that the ionospheric supply is the escape limiting factor.

Cusp escape is influenced by competing effects as the solar wind pressure increases. On the one side the solar wind energy flux increases, increasing the escape rate. On the other side the magnetospheric cross-section decreases, reducing the intercepted solar wind energy flux. As shown in Figure 4, the increase of the solar wind energy flux dominates, and the amount of solar wind energy deposited in the cusp region increases, thus the cusp escape rate increases as the solar wind pressure increases. Meanwhile, Earth's magnetic moment also plays a dual role: as the Earth's magnetic moment increases, the magnetospheric cross section with the solar wind increases allowing more solar wind energy to be deposited in the cusp region. Consequently, the cusp escape rate increases. However, a stronger magnetic moment also shrinks the cusp size resulting in a higher escape flux that can deplete the available oxygen ions to escape. Once escape saturation is reached, the flux of escaping oxygen remains constant and the total cusp escape rate only varies with the surface of the cusp region.

Therefore the Earth's magnetic moment has a double effect on cusp escape (magnetospheric cross-section and cusp size), leading to a mechanism that is more sensitive to the changes of the Earth's magnetic moment than polar wind, which has a single effect (polar cap size).

For the cross-field ion loss, there is small change due the variations of the solar wind pressure, and there are small fluctuations associated with changes in the Earth's magnetic moment.

The contributions from Jeans escape and Auroral Sputtering are significantly less than from polar wind escape (above $\sim 10^{25}$ s^{-1}), cusp escape

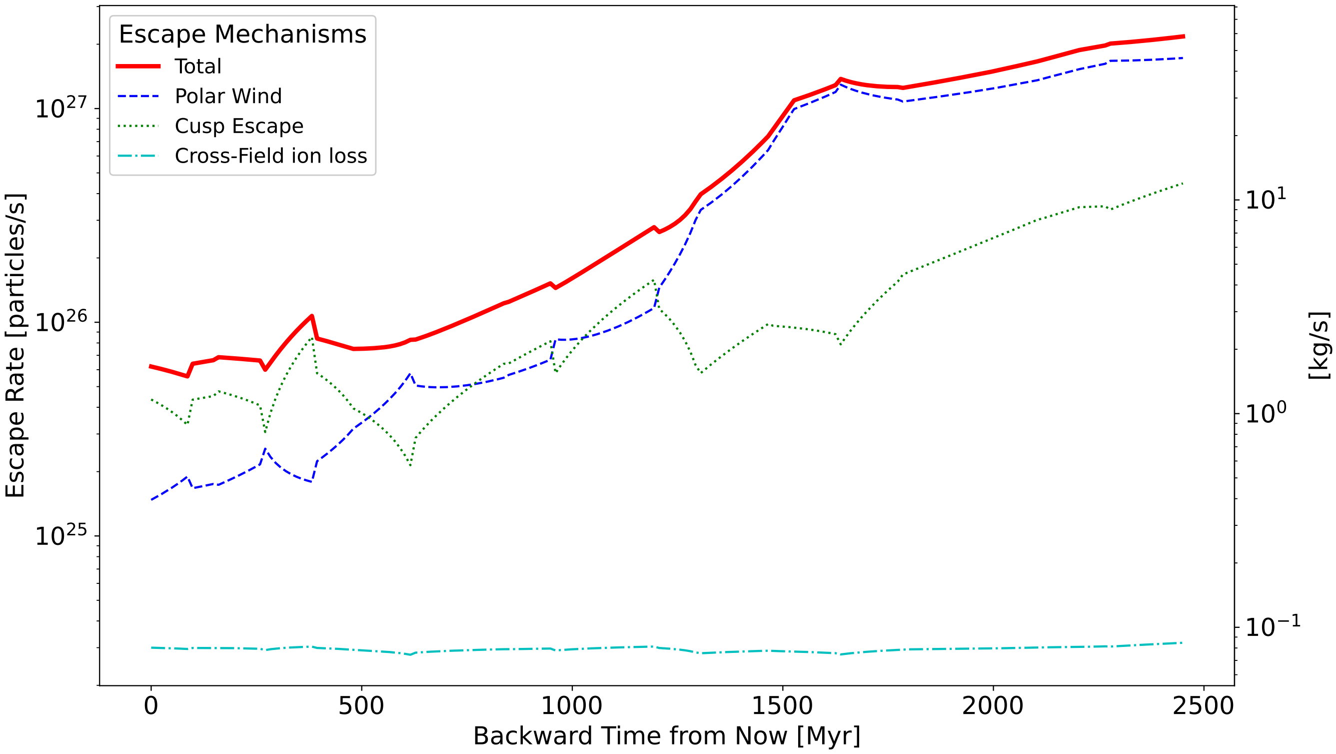

Figure 4: *Evolution of the main contributors to the total escape rate.*

(above $\sim 10^{25}$ s^{-1}), and cross-field ion loss, with a maximum particle flux contribution of 4.5 $\times 10^{13}$ s^{-1} and of 8×10^{23} s^{-1}, respectively. Auroral sputtering decreases with the exobase expansion, as the exobase density decreases.

Conclusions

This study estimates the evolution of the oxygen escape rates at Earth from different escape mechanisms for the last 2450 Myr. using a semi-empirical model. This model takes into consideration the combined effects of the changes on Earth's magnetic moment, solar wind pressure, solar EUV radiation and their effects on the Earth's exosphere in time to estimate the oxygen escape. We conclude that two mechanisms dominate the total oxygen escape rate: polar wind and cusp escape.
The estimated total oxygen mass loss during the last 2450 Myr. is $\sim 7 \times 10^{17}$ kg, which corresponds to 15% of the current atmospheric mass or 63% of the current atmospheric oxygen mass. This seems a large oxygen loss but it is less substantial than the oxygen released to the atmosphere due to the GOE, and it didn't drastically change the atmospheric content. Our oxygen loss estimation is likely an upper limit, as we consider current and constant atmospheric composition in our exospheric model [Johnstone et al. 2018], when in fact if there was less oxygen at the exobase altitude in the past, ion escape would reach saturation sooner, reducing the oxygen loss.

The polar wind escape rate increases towards the past. The cusp escape rate increases with a more mild variation, due to the compression of the magnetosphere when the solar wind pressure increases. This reduces the cross section of the magnetosphere with the solar wind and attenuates the increase of the solar wind energy deposition in the cusp region associated with increase of the solar wind energy flux. Moreover cusp escape is more sensitive to Earth's magnetic moment variations. Other escape mechanisms do not contribute significantly to Earth's total oxygen loss.

We conclude that an increasing solar wind pressure increases the oxygen escape rate for a magnetised planet. However, the planetary magnetic moment has a complex relationship with oxygen escape, because it affects diverse mechanisms differently. For a magnetised planet, like Earth, the increase of the planetary magnetic moment is associated with an increase of the cusp escape rate and a reduction of the polar wind rate. A large-scale magnetosphere does not necessarily protect the planet from atmospheric escape, due to ion escape in the polar regions.

This work shows that atmospheric escape is a complex phenomenon with key parameters that determine the ability of any magnetised planet (including extrasolar planets) to retain its atmosphere: the stellar wind pressure and its magnetic moment. Exospheric parameters as the exobase altitude and the ionospheric supply, also affect the atmospheric escape from any magnetised planet. The lower boundary of our model is used to parametrize the areas where different escape mechanisms take place (e.g: polar cap area at exobase altitude). The ionospheric supply determines the maximum escape flux from a mechanism, saturating the escape rate. Other characteristics, such as planetary rotation or planetary atmospheric composition, need further research to estimate their contribution to atmospheric loss.

It is difficult to extrapolate the oxygen escape rate calculations to extrasolar planets, as the semi-empirical model is based on the extrapolation of measurements made at Earth. Oxygen escape rate estimations would be possible only for extrasolar planets very similar to Earth (in terms of atmosphere, mass, and with an intrinsic magnetic field) and in a similar stellar environment to the Sun (in terms of stellar EUV radiation). Nonetheless, the understanding of atmospheric escape presented above applies to a broader range of magnetised extrasolar planets.

References

[Barakat et al. 1987] Barakat, A. R. and Schunk, R. W. and Moore, T. E. and Waite, J. H. (1987). Ion Escape Fluxes From the Terrestrial High-Latitude Ionosphere. *Journal of Geophysical Research*, 92:12255–12266.

[Bono et al. 2022] Bono, R. K. and Paterson, G. A. and van der Boon, A. and Engbers, Y. A. and Grappone, J. M. and Handford, B. and Hawkins, L. M. A and Lloyd, S. J. and Sprain, C. J. and Thallner, D. and Biggin, A. J. (2022). The PINT database: a definitive compilation of absolute palaeomagnetic intensity determinations since 4 billion years ago. *Geophysical Journal International*, 229:522–545.

[Carolan et al. 2019] Carolan, S. and Vidotto, A. A. and Loesch, C. and Coogan, P. (2019). The evolution of Earth's magnetosphere during the solar main sequence. *Monthly Notices of the Royal Astronomical Society*, 489:5784–5801.

[Gunell et al. 2018] Gunell, H. and Maggiolo, R. and Nilsson, H. and Stenberg Wieser, G. and Slapak, R. and Lindkvist, J. and Hamrin, M. and De Keyser, J. (2018). Why an intrinsic magnetic field does not protect a planet against atmospheric escape. *Astronomy & Astrophysics*, 614:L3.

[Gronoff et al. 2020] Gronoff, G. and Arras, P. and Baraka, S. and Bell, J. M. and Cessateur, G. and Cohen, O. and Curry, S. M. and Drake, J. J. and Elrod M. and Erwin, J. and Garcia-Sage, K. and Garraffo, C. and Glocer, A. and Heavens, N. G. and Lovato, K. and Maggiolo, R. and Parkinson, C. D. and Simon Wedlund, C. and Weimer, D. R. and Moore, W. B. (2020). Atmospheric escape processes and planetary atmospheric evolution. *Journal of Geophysical Research: Space Physics*, 125:1–77.

[Johnstone et al. 2018] Johnstone, C. P. and Güdel, M. and Lammer, H. and Kislyakova, K. G. (2018). Upper atmospheres of terrestrial planets: Carbon dioxide cooling and the Earth's thermospheric evolution. *Astronomy & Astrophysics*, 617:A107.

[Lundin et al. 2007] Lundin, R. and Lammer, H. and Ribas, I. (2007). Planetary Magnetic Fields and Solar Forcing: Implications for Atmospheric Evolution. *Space Science Reviews*, 129:245-278.

[Nilsson 2011] Nilsson, H. (2011). Heavy Ion Energization, Transport, and Loss in the Earth's Magnetosphere. *The Dynamic Magnetosphere*, 3:315–327.

[Ramstad & Barabash 2021] Ramstad, R. and Barabash, S. (2021). Do Intrinsic Magnetic Fields Protect Planetary Atmospheres from Stellar Winds. *Space Science Reviews*, 217:1–39.

[Ribas et al. 2005] Ribas, Ignasi and Guinan, Edward F. and Güdel, Manuel and

Audard, Marc (2005). Evolution of the Solar Activity over Time and Effects on Planetary Atmospheres. I. High-Energy Irradiances (1-1700 Å). *The Astrophysical Journal*, 622:680–694.

[Schillings et al. 2018] Schillings, A. and Nilsson, H. and Slapak, R. and Wintoft, P. and Yamauchi, M. and Wik, M. and Dandouras, I. and Carr, C. M. (2018). O+ Escape During the Extreme Space Weather Event of 4–10 September 2017. *Space Weather*, 16:1363–1376.

Non-perturbative modelling of the tidal force and apsidal motion in close binary systems

L. Fellay[1] & **Young Minds Liège**[1]

[1] *STAR Institute, University of Liège, 19C Allée du 6 Août, B−4000 Liège, Belgium*

Stellar deformations play a significant role in the dynamical evolution of stars in binary systems, impacting the tidal dissipation and the outcomes of mass transfer processes. The prevalent method for modelling the deformations and tidal interactions of celestial bodies solely relies on the perturbative approach, which assumes that deformations are minor perturbations of the spherical symmetry. An observable consequence to stellar deformations is the apsidal motion (i.e. the precession of the line connecting the apsides of an eccentric orbit) which has been observationally quantified across numerous binary systems. In this work, we provide an overview of our recent findings from [Fellay et Dupret 2023], in which we present a novel non-perturbative approach to model the deformations of binaries in 3D, obtaining the tidal force and the consequent apsidal motion. In this review, we develop both the pertubative and the non pertubative modelling approaches. Furthermore, we investigate the reliability of the perturbative approach when used to model close and deformed binary systems. Our work showed that the perturbative approach systematically underestimates tidal interactions between stars. All the subsequent modelling is impacted by our findings, in particular, the tidal dissipation is significantly underestimated. As a result, all the current binary stellar models are lack precision when applied to systems with short orbital separation, and the outcomes of these models are also affected by these inaccuracies.

1 Introduction

Binary stars are pairs of gravitationally bound stars. They constitute a significant fraction of observed stellar population, during the Data Realese 3 from the *Gaia* spacecraft [Gaia Collaboration et al., 2020], more than $800,000$ stars in non-single systems were catalogue [Gaia Collaboration 2022], representing $\sim 20\%$ of the total catalogue. In particular, high mass stars ($M_\star > 8$ solar mass ($M_\odot$)) have higher occurrence in binary systems. It is estimated that over 70% of massive stars are impacted during their evolution by an interaction with a companion [Sana et al., 2012]. Similarly, intermediate-mass stars ($2M_\odot > M_\star > 8M_\odot$) are frequently observed in binary configurations [Torres et al., 2010, Claret et al, 2021, Marcussen & Albrecht, 2022]. In opposition, low mass stars ($M_\star < 2M_\odot$) are less commonly observed in binaries although this observation may be subject to an observational bias linked to the faintness of these bodies.

In binary systems, the presence of a nearby companion influence the conventional evolutionary path of each constituent star. A common phenomenon in binaries is the Roche-lobe overflow

where a star transfers material and angular momentum to its companion. This transfer induces substantial modifications in the evolutionary paths of both binary components, affecting their respective masses and angular momentum. As the system evolves, orbital migration can occur and lead to phases of common envelope characterized by a contact between the envelopes of the two stars, resulting in the exchange of angular momentum and chemicals. Before reaching these critical stages, stars experience deformations as a consequence of their mutual interactions, predominantly governed by the gravitational, tidal, and centrifugal forces.
Tidal forces within binary systems are the consequence of gravitational interactions between non-punctual celestial bodies. They can be subdivided into two distinct components: equilibrium tides, which arise from the large-scale circulation resulting from a hydrostatic readjustment (i.e., stellar deformations), and dynamical tides [Sterne 1939], which correspond to the excitation of eigenmodes of oscillations due to the periodic perturbations imposed by a companion. These tidal forces and the resulting stellar deformation lead to various phenomena such as orbital rotation synchronisation, mass transfer, and tidal dissipation, the latter corresponding to the dissipation of orbital energy within the stellar bodies.

Apsidal motion is characterized by the temporal variation of the argument of periastron, denoted as ω, this orbital parameter is illustrated in Figure 1. Apsidal motion represents the motion the apsidal line in eccentric binary systems (see Figure 1). Apsidal motion originates from equilibrium tides, dynamical tides [Willems & Claret, 2002] and corrections from general relativistic effects [Gimenez 1985]. It serves as an observational constraint for understanding the structure of deformed stars, providing insights into the microphysics of stellar models. Accurate modelling of tidal and centrifugal deformations is essential for determining the precise stellar structure of each component in binary systems and to link the observed apsidal motion to a direct constrain on the stellar structure.

In the modelling of the structure and deformations of binary stars, the perturbative approach is one of the most sophisticated and widely used method in the literature. The underlying principle of this methodology is to treat deformations as small perturbations of the spherical symmetry of stars, only accounting for the leading orders terms in the developments. This approach allows for obtaining simplified structural deformations from the unperturbed spherically symmetric structure.

In this review, we start by introducing the basic formalism of the perturbative approach in section 2. Then, in section 3 we develop the formalism used by our non-perturbative modelling. In section 4, we compare the two modelling approaches for a specific observed binary systems before discussing, in section 5, the implication of our studies for current models strategies used in the literature.

2 Perturbative modelling of the tidal force

In a binary system, the radial relative acceleration of two bodies given by the classical celestial mechanics is

$$\frac{F_{21}}{m_\mu} = -\frac{GM_1M_2}{r^2} + F_\mathrm{R}, \tag{1}$$

where F_{21} is the force exerted by the secondary star on the primary (noting $F_{2\to 1} \equiv F_{21}$), M_1 and M_2 are the masses of the stars, F_R is the perturbed acceleration resulting from considering stars as non-spherical extended rotating interacting bodies, and m_μ is the reduced mass of the system defined as

$$m_\mu = \frac{M_1M_2}{M_1+M_2}. \tag{2}$$

This perturbation is responsible for all the equilibrium tidal-induced dynamical effects of binary evolution, including orbital migration (i.e. variation of systems semi-major axis), eccentricity dissipation (i.e. reduction of orbital eccentricty), and apsidal motion (i.e. time variation of the argument of the periastron). Figure 1 illustrates the orbital parameters of an eccentric binary system, the apsidal motion being denfined as $\mathrm{d}\omega/\mathrm{d}t$. When wanting to model the perturbed acceleration originating from both tidal and centrifugal forces, a modelling approach must be selected. The most commonly employed method in the literature is the perturbative method, which assumes that

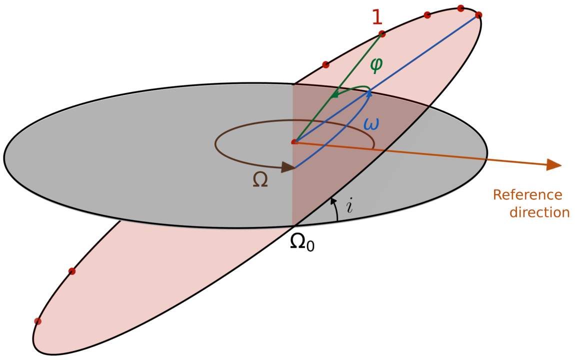

Figure 1: *Orbital trajectory of a star in a binary system around its center of mass. The orbit has an eccentricity e of* 0.2*. The orbital plane is in red, the gray plane is a the reference plane (i.e. the plane of the sky), i is the inclination of the system compared to the reference plane,* Ω *is the longitude of the ascending node,* Ω_0 *is the ascending node,* ω *is the argument of the periastron, and* φ *is the true anomaly. This figure is extracted from [Fellay et al., 2023].*

the deformations of the stars are small compared to their radii. In practical terms, this means that only the first-order terms are considered in derivations. By making this assumption, the stellar deformations and the stellar perturbed structure can be obtained from the unperturbed structure by solving the well-known Clairaut-Radau first order differential equation:

$$\bar{r}\frac{\mathrm{d}\eta_\ell}{\mathrm{d}\bar{r}} + 6\frac{\rho(\bar{r})}{\bar{\rho}(\bar{r})}(\eta_\ell + 1) + \eta_\ell(\eta_\ell - 1) = \ell(\ell+1), \quad (3)$$

using the boundary conditions $\eta_\ell(0) = \ell - 2$. In the Clairaut-Radau equation $\bar{r}$ is the averaged radius of a stellar layer, ρ is its density, $\bar{\rho}$ the average density under the selected layer and ℓ is the spherical order considered of η_ℓ, which is defined as the logarithmic derivative of the radial deformation projected onto a spherical harmonics basis. Solving this equation allows us to determine the radial deformation, η_ℓ, for each star when subjected to a perturbing potential. The non-spheroidal response of a celestial body's surface to a perturbation is ultimately linked to the perturbing potential through the apsidal motion constants, which are defined as follows

$$k_{\ell,1} = \frac{1 + \ell - \eta_{1\ell}(R_1)}{2(\eta_{1\ell}(R_1) + \ell)}, \quad (4)$$

where R_1 and R_2 are the surface of the stars as given by the unperturbed structure. Physically, $k_{\ell,1}$ can be interpreted as a measure of a body surface deformability when subjected to an external potential. The perturbation of the surface gravitational potential of a star induced by its companion is ultimately expressed by the following equation:

$$\Psi^m_{1\ell}(R_1) = 2k_{\ell,1}\left(\Psi^m_{2,\ell}(R_1) + \Psi^m_{\mathrm{c},\ell}(R_1)\right) \quad (5)$$

where $\Psi^m_{2,\ell}(R_1)$ is the perturbing gravitational potential evaluated at the surface of the star considered and $\Psi^m_{\mathrm{c},\ell}(R_1)$ is the centrifugal potential. For these expression to be valid, the structure of our stars have to be batropic, signifying that all considered forces must originate from a potential. To satisfy this requirement, the rotation of stars must exhibit cylindrical symmetry. In this study, we simplify the problem further by assuming that stars have solid-body rotations, a justification of this assumption is given is section 5.

The perturbative theory predicts that the dipolar component of the total potential is null when the secondary is treated as a point-mass, as gravitational and centrifugal forces cancel out, according to the third Kepler law. Therefore, the dominant term of the potential is the quadrupolar term ($\ell = 2$).

The perturbed acceleration can be decomposed as

$$F_\mathrm{R} = -\frac{1}{m_\mu}\left[F_{2'10} + F_{201'} + F_{2'1'}\right], \quad (6)$$

where $F_{2'10}$ is the force exerted by the quadrupolar deformation of the secondary on the unperturbed primary, $F_{201'}$ is the force exerted by the unperturbed secondary on the already perturbed primary, and $F_{2'1'}$ is the force exerted by the perturbed secondary on the already perturbed primary. The last term, $F_{2'1'}$, is a second order term, thus neglected in the pertubative approach. With third Newton's law, $F_{2'10} = F_{102'}$, these forces can be obtained by computing the derivative of the dipolar potential perturbation from the quadruplar deformation evaluated at the center of each star. The expression of the perturbed acceleration is finally :

$$F_\mathrm{R} = -2\frac{GM_\mathrm{tot}}{r^2}\left[k_{2,2}\frac{1}{q}\left(\frac{R_2}{r}\right)^5\left(3 + \frac{q+1}{2}\left(\frac{\Omega_{\star,2}}{\tilde{n}}\right)^2\right)\right. \quad (7)$$

$$\left. + k_{2,1}q\left(\frac{R_1}{r}\right)^5\left(3 + \frac{1}{2}\frac{q+1}{q}\left(\frac{\Omega_{\star,1}}{\tilde{n}}\right)^2\right)\right],$$

with $q = M_2/M_1$, $\Omega_{\star,1}$ and $\Omega_{\star,2}$ are respectively the primary and secondary star' rotation rate, and $\tilde{n}$ is the orbital mean rotation rate. The tidal component of the apsidal motion of an eccentric system is linked to the perturbed acceleration by the Gauss planetary equation :

$$\dot{\omega}_N \equiv \frac{\mathrm{d}\omega_N}{\mathrm{d}t} = -\frac{\sqrt{1-e^2}}{e}\sqrt{\frac{a}{GM_{\mathrm{tot}}}}\langle F_{\mathrm{R}} \cos\varphi\rangle, \quad (8)$$

where M_{tot} is the total mass of the binary system and $\langle F_{\mathrm{R}} \cos\varphi\rangle$ is orbital time averaged perturbed acceleration. The tidal component of the apsidal motion of an eccentric binary system is finally obtained by computing the time average perturbed acceleration and is given by

$$\begin{aligned}\frac{\mathrm{d}\omega_N}{\mathrm{d}t} = \frac{2\pi}{P_{\mathrm{orb}}}\Bigg[15f(e)\left(\left(\frac{R_1}{a}\right)^5 qk_{2,1} + \left(\frac{R_2}{a}\right)^5 \frac{k_{2,2}}{q}\right) \quad (9)\\ + g(e)\left(k_{2,1}(q+1)\left(\frac{P_{\mathrm{orb}}}{P_{\star,1}}\right)^2\left(\frac{R_1}{a}\right)^5\right.\\ \left. + k_{2,2}\frac{q+1}{q}\left(\frac{P_{\mathrm{orb}}}{P_{\star,2}}\right)^2\left(\frac{R_2}{a}\right)^5\right)\Bigg],\end{aligned}$$

with,

$$f(e) = \frac{1+\frac{3}{2}e^2+\frac{1}{8}e^4}{(1-e^2)^5}, \quad (10)$$

and,

$$g(e) = \frac{1}{(1-e^2)^2}. \quad (11)$$

A more thoroughly derivation of this formalism can be found in [Kopal 1978, Fellay et al., 2023]. When observing eclipsing binary systems with low inclination, the radii can be obtained with high precision ($\sigma < 1\%$), the orbital period can be determined as well as the mass ratio of the binary stars, the eccentricity of the system and the stellar rotation periods. By observing the apsidal motion of a system, a constrain can therefore be drawn on the stellar structure through the k_2 coefficient of each star. The apsidal motion of eccentric binaries has already been observed for a significant amount of systems [Wolf et al., 2006, Wolf et al., 2008, Wolf et al., 2010, Torres et al., 2010, Rosu et al., 2020b, Baroch et al., 2021, Baroch et al., 2022, Claret et al, 2021, Marcussen & Albrecht, 2022, Rosu et al., 2022a, Rosu et al., 2022b, Rosu et al., 2023]. Consequently, constraints on the stellar structure can be obtained for each of these systems. It's important to note that due to the degeneracy of contributions from both stars (see Equation 9), apsidal motion alone cannot be employed to exclusively constrain a single star's structure in a system. However, in the case of twin binary systems, which are systems composed of stars with identical stellar properties, the constraint on apsidal motion directly translates into a constraint on the stellar structure. This approach can be effectively employed to probe the microphysics underlying our stellar models. This was done for example in [Rosu et al., 2020b, Rosu et al., 2022a, Rosu et al., 2022b, Rosu et al., 2023].

As previously mentioned, the apsidal motion also has a component linked to general relativistic corrections [Gimenez 1985] expressed as:

$$\frac{\mathrm{d}\omega_{\mathrm{rel}}}{\mathrm{d}t} = \frac{2\pi}{P_{\mathrm{orb}}}\frac{3G(M_1+M_2)}{c^2a(1-e^2)}. \quad (12)$$

The total apsidal motion of a system is simply the sum of two components:

$$\dot{\omega} = \dot{\omega}_N + \dot{\omega}_{\mathrm{rel}}. \quad (13)$$

3 3D non-perturbative modelling of the tidal force and apsidal motion

In our recent works [Fellay et Dupret 2023, Fellay et al., 2023], we developed a tool called MoBiDICT, designed to model close binaries using a non-perturbative approach to treat the deformations. Our method iteratively solves the Poisson equation ($\Delta\Psi = 4\pi G\rho$) on a 3D structure, allowing to obtain the gravitational and tidal potential and deformations accounting for the redistribution of mass within the bodies. MoBiDICT uses conservative nature of all the forces considered, resulting in a barotropic model structure (i.e. the densities are constant on equipotentials). By assuming that in a given direction ($\mu_{\mathrm{crit}}, \phi_{\mathrm{crit}}$) each star is described by a 1D spherically symmetric input model, we can recompose the entire 3D density profile from the total potential ($\Psi_{\mathrm{tot}} = \Psi_1 + \Psi_2 + \Psi_{\mathrm{c}}$) of each star. This method is thoroughly explained in [Fellay et Dupret 2023]. Figure 2 illustrates the orbital configuration and deformations of a binary system modelled with our 3D on-perturbative

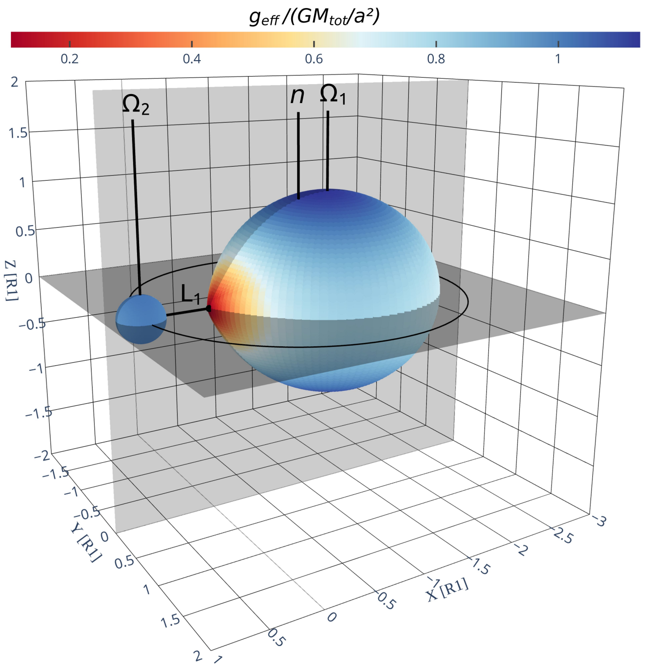

Figure 2: *Binary system configuration with non-synchronised rotations. The system is composed of 1 $M_\odot$ Main-Sequence (MS) primary star and a 0.2 $M_\odot$ MS companion separated by $r = 2R_1$. The two grey planes are the planes of symmetry of the systems, each rotation axis is marked with a black line. The orbital rotation is originating from the system centre of mass, located inside the primary. The color code corresponds to the surface effective gravity, the local flux emitted by a star being a function of this quantity. This figure is extracted from [Fellay et al., 2023]*

method. The output obtained from our modelling method are the gravitational potentials and densities projected on spherical harmonics basis:

$$\rho_i(r_i, \mu, \phi) = \sum_{\ell=0}^{L} \sum_{k=0}^{(\ell-p)/2} \rho^m_{i,\ell}(r_i) Y_{\ell,m}(\mu, \phi), \quad (14)$$

and

$$\Psi_i(r_i, \mu, \phi) = \sum_{\ell=0}^{L} \sum_{k=0}^{(\ell-p)/2} \Psi^m_{i,\ell}(r_i) Y_{\ell,m}(\mu, \phi), \quad (15)$$

where L is the free parameter of our modelling defining the maximum degree of the spherical harmonics to be accounted for, $p = 0$ if ℓ is even, $p = 1$ otherwise, and $m = 2k + p$. Formally, the force excerted by the secondary on the primary star is

$$F_{21} = -\int \rho_1 \frac{\partial \Psi_2}{\partial x} dV_1, \quad (16)$$

By decomposing the densities and the forces in unperturbed spherical symmetric terms, respectively ρ_{10} and F_{20}, and non-spherical perturbations, respectively ρ_1' and F_2', the force exerted by the secondary on the primary can be rewritten as

$$F_{21} = -\int (\rho_{10} + \rho_1')(F_{20} + F_2')\, dV_1. \quad (17)$$

Within our formalism, the perturbed force is obtained from the non-spherically symmetric terms of these expansions, all the terms with $\ell \geq 1$. Formally, the force exerted by the secondary on the primary star only considering the non-spherically symmetric terms can be rewritten as

$$\begin{aligned} F_R = &-\frac{1}{m_\mu} \int \rho^0_{1,0} Y_{0,0} \left(\sum_{\ell=1}^{L} \sum_{k=0}^{(\ell-p)/2} F^m_{2,\ell} \right) dV_1 \quad (18) \\ &- \frac{1}{m_\mu} \int \left(\sum_{\ell=1}^{L} \sum_{k=0}^{(\ell-p)/2} \rho^m_{1,\ell} Y_{\ell,m} \right) F^0_{2,0} dV_1 \\ &- \frac{1}{m_\mu} \int \left(\sum_{\ell=1}^{L} \sum_{k=0}^{(\ell-p)/2} \rho^m_{1,\ell} Y_{\ell,m} \right) \left(\sum_{\ell=1}^{L} \sum_{k=0}^{(\ell-p)/2} F^m_{2,\ell} \right) dV_1. \end{aligned}$$

with,

$$F^m_{2,\ell} = \frac{\partial r_1}{\partial x_1} \frac{\partial \Psi^m_{2,\ell} Y_{\ell,m}}{\partial r_1} + \frac{\partial \theta_1}{\partial x_1} \frac{\partial \Psi^m_{2,\ell} Y_{\ell,m}}{\partial \theta_1} + \frac{\partial \phi_1}{\partial x_1} \frac{\partial \Psi^m_{2,\ell} Y_{\ell,m}}{\partial \phi_1}. \quad (19)$$

In Equation 19, $\Psi^m_{2,\ell} Y_{\ell,m}$ are quantities depending on the grid of the secondary (r_2, μ_2, ϕ_2), the expression of their derivative with respect to the grid of the primary star can be found in [Fellay et Dupret 2023].

To obtain the tidal contribution to the apsidal motion, the time average of the perturbed acceleration have to be computed (see Equation 8). To achieve this with our non-pertubative methodology, we are taking snapshots of stellar deformation at different point of the orbit to compute the orbital time average. With this method, merely 15 snapshots taken over half of an orbit is sufficient to obtain a relative precision of 10^{-5} on the apsidal motion.

4 Comparison between perturbative et non-pertubative modelling

The non-pertubative and pertubative approaches can be compared on different points. The apsidal motion is a direct constraint on the modelling discrepancies and the underlying perturbed acceleration difference. In this review, we have chosen to focus on a specific observed twin binary system composed of intermediate mass stars, called PV-Cas [Torres et al., 2010, Claret et al, 2021, Marcussen & Albrecht, 2022], whose properties are detailed in Table 1. Using the Code Liégeois d'Evolution Stellaire [Scuflaire et al., 2006, CLES] we built 1D stellar models reproducing all properties of the observed twin binary systems and using the apsidal motion as constrain on the stellar structure. With the model obtained, we investigated the discrepancy in F_R between the perturbative and non-perturbative approaches as a function of the binary separation r, this difference is illustrated in Figure 3. In this figure, we decomposed the perturbed acceleration discrepancy with the spherical harmonics use to compute each component (see Equation 18). For the perturbative approach only the dominant terms (the quadropular terms) were taken, as justified in section 2 while with our formalism all the spherical harmonics were accounted for. Generally, at low orbital separations, the corrections arising from non-perturbative modelling start to become non-negligible, in this case a perturbed acceleration discrepancy of 13% can be seen before the contact of the binaries. A closer examination of the $\ell = 2$ terms of the decomposition in Figure 3 reveals that most of the discrepancies are originating from the $\ell = 2, m = 2$ term. In the $\ell = 2, m = 0$ term both tidal force and centrifugal force are included while in the $\ell = 2, m = 2$ term only the tidal force in present. This suggests that the perturbative approach lacks precision when modelling tidal forces at low orbital separations. In total, the quadrupolar terms contribute to approximately 40% of the discrepancies seen. Moreover, with our formalism the dipolar component is non-null and contributes for approximately a quarter of the total discrepancies. The $\ell = 3$ components are finally contributing for 35% of the discrepancies, while higher order terms have near negligible contributions. In terms of apsidal motion, for the system PV-Cas with the observed orbital parameters, the contribution from non-perturbative modelling reaches 3%. This correction is of the same order of magnitude as the general relativistic corrections. By adding the non-perturbative corrections to the apsidal motion into the stellar modelling procedure we saw that the stellar model required more extra mixing to reproduce the apsidal motion. The extra mixing in stellar interior corresponds to a transport of chemicals and angular momentum, therefore needing extra mixing signify that a process acts in stellar interior to transport material. As [Rosu et al., 2020b, Rosu et al., 2022a, Rosu et al., 2022b, Rosu et al., 2023] showed, the extra mixing required to reproduce the observed apsidal motion of several systems was already important, our modelling did not correct this effect but rather exacerbated it. The missing transport process could be linked to rotations or propagations of waves within the stellar interior.

Table 1: *Orbital and stellar properties of the PV-Cas system.*

Stellar Properties	
M[$M_\odot$]	2.78±0.08
R[$R_\odot$]	2.28±0.04
$T_{\mathrm{eff}}[K]$	10200±250
P_{orb} [days]	1.7504698±0.0000009
i [°]	85.8
e	0.0325±0.0005
$P_\star/P_{\mathrm{orb}}$	1.0±0.1
$\dot{\omega}$ [°cycle^{-1}]	0.0212±0.0002

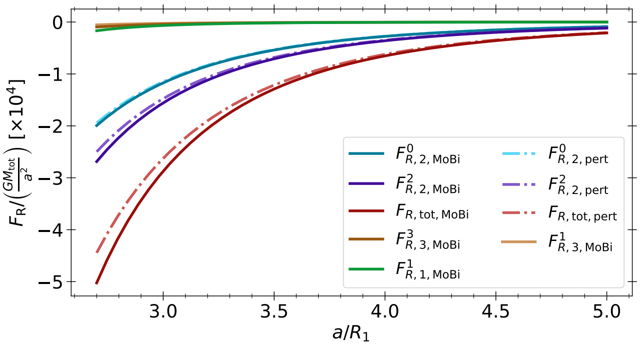

Figure 3: *Decomposition of the perturbed acceleration for the PV-Cas system with the perturbative and non-perturbative models as a function of the system orbital separation normalised by the stellar radii. The $y-axis$ is the pertubed acceleration normalized by a constant of the system, each color represents one spherical order: the lighter curves correspond to the perturbative model while the darker curves correspond to the with non-perturbative approach. The red curves are the total of all the spherical orders.*

More comparisons between the two modelling techniques can be found in [Fellay et al., 2023].

5 Discussion and Conclusion

In our comparison of the two modelling methods in [Fellay et al., 2023], we determined that for an orbital separation of $a(1-e^2)/R_1 < 6.5$ a discrepancy of at least 2% can be found in the apsidal motion for any type binary system. To assess implication of our results on the population of observed binaries with apsidal motion, we constructed a comprehensive catalogue of such systems. In total, our catalogue includes 61 systems, encompassing all systems with constraints on their stellar parameters and observed apsidal motion found in the literature. These systems were obtained by merging two recent catalogues of observed binary systems [Claret et al, 2021, Marcussen & Albrecht, 2022] with apsidal motion to systems from various literature sources [Wolf et al., 2006, Wolf et al., 2008, Wolf et al., 2010, Torres et al., 2010, Rosu et al., 2020b, Baroch et al., 2021, Baroch et al., 2022, Rosu et al., 2022a, Rosu et al., 2022b, Rosu et al., 2023] where determinations of stellar and orbital parameters were available. In Figure 4 we illustrate the tidal contribution to the apsidal motion against the parameter $a(1-e^2)/R_1$ of each observed system of the catalogue. At short orbital separations, the apsidal motion is dominated by the tidal component, while at high orbital separation the systems are observed with an apsidal motion primarily due to the contributions of general relativity. Given that most of the uncertainties in the modelling can be attributed to the tidal component, systems with a low tidal contribution to the apsidal motion yield worst constraints on the stellar structure. This increase in uncertainties at high orbital separation is illustrated with the error bars in Figure 4. Consequently, systems with low orbital periods provide the most reliable constraints on the stellar structure. Our results demonstrates that, particularly at short orbital periods, the conventional approaches to modelling tidal perturbations and apsidal motion lack precision, introducing biases into studies conducted for these systems. Approximately 40% of the observed systems in our catalogue have at least a 2% correction of the apsidal motion from the non-perturbative modelling, a correction greater than the uncertainties from observations. For the low-mass stars, we showed in [Fellay et al., 2023] that these discrepancies can reach up to 70% and 45% for evolved intermediate mass stars.

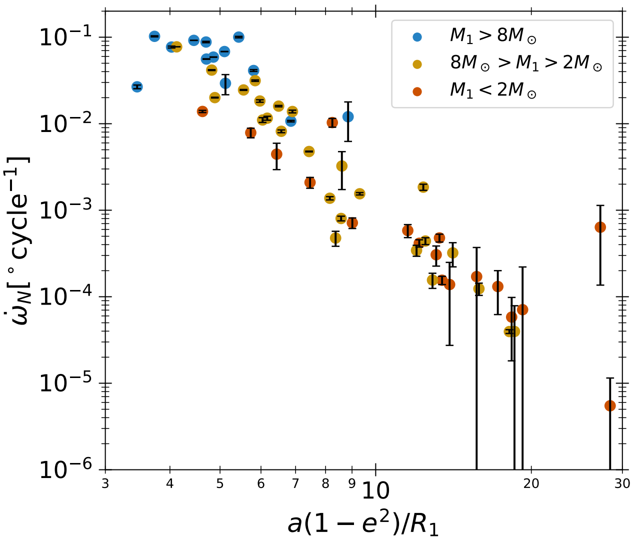

Figure 4: *Repartition of the tidal contribution to the apsidal motion as a function of the orbital separation of the observed binary systems from our catalogue. The blue dots correspond to massive binaries, the yellow points are intermediate mass binary stars, and the red dots are low-mass stars. For this diagram, the primary was chosen as the most massive star in the system.*

The discrepancies observed between our non-perturbative method and classical modelling procedures do not only affect the apsidal motion but also all the orbital dynamics of the system. Given the underestimation of the tidal force, all aspects of stellar evolution are influenced by an underestimation of tidal dissipation, and consequently the tidal orbital migration and circularisation. Such modifications in the dynamical interactions of binary systems can directly impact the remnants of massive binary systems, influencing our understanding of the formation processes of close binary black holes. Consequently, our work has the potential to significantly influence the outcomes of population synthesis studies, as these studies are closely tied to the physics of stellar interactions.

Another main implication of our work concerns the modelling and understanding of mass transfer and phases of common envelope in binary systems. Such systems are in the regime were non-perturbative corrections are most significant, introducing variations in the tidal force of at least tens of percent. The modelling of these phases is already dependent on many free parameters, additional uncertainties in the classical models is predicted by our modelling during these crucial phases of binary evolution. In the future, our non-perturbative approach could be adapted to model the structure and interactions of contact binaries.

One of the primary limitations of both our method and perturbative models is the assumption of solid-body rotation. For single stars, such an assumption is not always justified as differential rotation appears and changes along with stellar evolution. However, in binary systems, as mentioned earlier, significant extra mixing appears due to stellar interactions, reducing the differential rotation in interacting bodies. The subject of angular momentum transport processes in binary systems is a complex and extensive area of research that warrants further investigation.

Acknowledgements: Loïc Fellay was supported by the Fonds de la Recherche Scientifique F.R.S.-FNRS as a Reaserch Fellow. Young Minds Liège is supported by activity-oreinted grants from the European Physical Society for outreach and science diffusion events.

References

[Baroch et al., 2021] Baroch, D. and Giménez, A. and Ribas, I. and Morales, J. C. and Anglada-Escudé, G. and Claret, A., Analysis of apsidal motion in eclipsing binaries using TESS data. I. A test of gravitational theories, A&A, 2021,649, A64.

[Baroch et al., 2022] Baroch, D. and Giménez, A. and Morales, J. C. and Ribas, I. and Herrero, E. and Perdelwitz, V. and Jordi, C. and Granzer, T. and Allende Prieto, C.,Absolute dimensions and apsidal motion of the eclipsing binaries V889 Aquilae and V402 Lacertae, A&A, 2022,665,A13.

[Claret et al, 2021] Claret, A. and Giménez, A. and Baroch, D. and Ribas, I. and Morales, J. C. and Anglada-Escudé, G.,Analysis of apsidal motion in eclipsing binaries using TESS data. II. A test of internal stellar structure, A&A, 2021,654, A17.

[Fellay & Dupret, 2023] Fellay, L. and Dupret, M. -A., MoBiDICT: New 3D static models of close synchronised binaries in hydrostatic equilibrium, A&A, 2023, 676,A22.

[Fellay et al., 2023] Fellay, L. , Dupret, M. -A. and S.Rosu, Underestimation of the tidal force and apsidal motion in close binary systems by the perturbative approach: comparisons with non-perturbative models,arXiv e-prints,2023.

[Gaia Collaboration et al., 2020] Gaia Collaboration and Brown, A. G. A. and Vallenari, A. and Prusti, T. and de Bruijne, J. H. J. and Babusiaux, C. and Biermann, M.,Gaia Early Data Release 3: Summary of the contents and survey properties,arXiv e-prints,2020.

[Gaia Collaboration 2022] Gaia Collaboration,VizieR Online Data Catalog: Gaia DR3 Part 3. Non-single stars (Gaia Collaboration, 2022), VizieR Online Data Catalog,2022.

[Gimenez 1985] Gimenez, A., General-relativistic periastron advances in eclipsing binary systems., APJ, 1985,297,405-412.

[Hut 1981] Hut, P.,Tidal evolution in close binary systems., A&A, 1981,99,126-140.

[Kopal 1978] Kopal, Z. Dynamics of close binary systems, 1978.

[Marcussen & Albrecht, 2022] Marcussen, Marcus L. and Albrecht, Simon H., The BANANA Project. VI. Close Double Stars are Well Aligned with Noticeable Exceptions; Results from an Ensemble Study Using Apsidal Motion and Rossiter-McLaughlin Measurements, APJ, 2022, 933,2, 227.

[Rosu et al., 2020a] Rosu, S. and Rauw, G. and Conroy, K. E. and Gosset, E. and Manfroid, J. and Royer, P., Apsidal motion in the massive binary HD 152248, A&A, 2020, 635,A145.

[Rosu et al., 2020b] Rosu, S. and Noels, A. and Dupret, M. -A. and Rauw, G. and Farnir, M. and Ekström, S., Apsidal motion in the massive binary HD 152248. Constraining the internal structure of the stars, A&A, 2020,642,A221.

[Rosu et al., 2022a] Rosu, S. and Rauw, G. and Farnir, M. and Dupret, M. -A. and Noels, A., Apsidal motion in massive eccentric binaries in NGC 6231. The case of HD 152219, A&A, 2022,660,A120.

[Rosu et al., 2022b] Rosu, S. and Rauw, G. and Nazé, Y. and Gosset, E. and Sterken, C., Apsidal motion in massive eccentric binaries: The case of CPD-41 7742, and HD 152218 revisited, A&A, 2022, 664,A98.

[Rosu et al., 2023] Rosu, S. and Quintero, E. A. and Rauw, G. and Eenens, P., New insight into the massive eccentric binary HD 165052: self-consistent orbital solution, apsidal motion, and fundamental parameters, MNRAS,2023,521,2,2988-3003.

[Sana et al., 2012] Sana, H. and de Mink, S. E. and de Koter, A. and Langer, N. and Evans, C. J. and Gieles, M. and Gosset, E. and Izzard, R. G. and Le Bouquin, J. -B. and Schneider, F. R. N.,Binary Interaction Dominates the Evolution of Massive Stars,Science,2012,337,6093,444.

[Scuflaire et al., 2006] Scuflaire, R. and Théado, S. and Montalbán, J. and Miglio, A. and Bourge, P.-O. and Godart, M. and Thoul, A. and Noels, A.,CLÉS, Code Liégeois d'Évolution Stellaire, APS, 2008, 316,83-91.

[Sterne, 1939] Sterne, T. E.,Apsidal motion in binary stars, MNRAS,1939,99,451-462.

[Torres et al., 2010] Torres, G. and Andersen, J. and Giménez, A., Accurate masses and radii of normal stars: modern results and applications, Astronomy and Astrophysics Reviews, 2010, 18, 1-2,67-126.

[Willems & Claret, 2002] Willems, B. and Claret, A.,The influence of dynamic tides on the apsidal-motion rate in close binaries with an evolved main-sequence star, A&A, 2002,382,1009-1015.

[Wolf et al., 2006] Wolf, M. and Kučáková, H. and Kolasa, M. and Štastný, P. and Bozkurt, Z. and Harmanec, P. and Zejda, M. and Brát, L. and Hornoch, K.,Apsidal motion in eccentric eclipsing binaries: CW Cephei, V478 Cygni, AG Persei, and IQ Persei, A&A, 2006,456,3,1077-1083.

[Wolf et al., 2008] Wolf, M. and Zejda, M. and de Villiers, S. N., Apsidal motion in southern eccentric eclipsing binaries: GL Car, QX Car, NO Pup and V366 Pup MNRS,2008,388,4,1836-1842.

[Wolf et al., 2010] Wolf, M. and Claret, A. and Kotková, L. and Kučáková, H. and Kocián, R. and Brát, L. and Svoboda, P. and Šmelcer, L., Relativistic apsidal motion in eccentric eclipsing binaries A&A 2010,509,A18.

[Zahn 1975] Zahn, J. -P.,The dynamical tide in close binaries., A&A,1975,41,329-344.

ACADEMIE ROYALE DES SCIENCES,
LETTRES ET DES BEAUX-ARTS
DE BELGIQUE

KONINKLIJKE VLAAMSE ACADEMIE DES
VAN BELGIË VOOR WETENSCHAPPEN
EN KUNSTEN

Organised by
National Committee for Pure and
Applied Physics
https://sites.google.com/view/bncpap/

March 21, 2026 / 09h30-17h20
Palais des Académies – Paleis der Academiën
Rue Ducale 1 Hertogstraat - Brussels

100 Years of Quantum Mechanics

PROGRAMME

09.00 Welcome of participants

09.30 Peter SCHLAGHECK : Introduction

09.40 Jean DALIBARD (Laboratoire Kastler Brossel, Collège de France, FR)
A Cool Journey Through Quantum Matter: 50 Years of Ultracold Atoms

10.30 Lieven VANDERSYPEN (QuTech, Technische Universiteit Delft, NL)
Quantum computing with electrons

11.20 Peter ZOLLER (University of Innsbruck & IQOQI, AT)
Quantum Simulation with Atoms and Ions

12.10 POSTER SESSION by the Belgian research institutions and **Lunch**

14.00 Christiane KOCH (Freie Universität Berlin, DE)
Training Schrödinger's cat: Quantum control in molecular physics and quantum information science

14.50 Vladan VULETIC (MIT, Boston, USA)
Quantum information and applications

15.40 Antoine BROWAEYS (Laboratoire Charles Fabry, Institut d'Optique, CNRS, Paris, FR)
Assembling quantum matter one atom at a time

16.30 Round-table discussion, animated by Frank VERSTRAETE (Universiteit Gent, BE)

17.20 Reception

Registration required before 10/03/2026 : https://forms.gle/d7h5fkH9t2N6pkif7.

Registration will be effective after receipt of the registration fee of 55 EUR*. Please make payment to account BE10 2500 0740 2704 of UNAMUR, with ref.: CPO 415610030 Colloquium 100 Years QM + your Name.

How to become a Member of the BPS

You want to become a Member of the Belgian Physical Society? Or to renew your membership?

For a new membership you can easily register by clicking on +*Register* on the front page (top right) of our website www.belgianphysicalsociety.be.

The fees for this year are:

- 60 € for ordinary members;
- 30 € for junior (<30) or senior (>65) members;

A lifetime BPS membership is possible as well, and the fee is 600 €.

Please pay the registration fee to the following bank account

IAN: BE03 0000 8457 3084; BIC: GEBABEBB
With the following communication: "BPS Membership" + year + your name.

Online payment on the BPS website is also possible.

Do not hesitate to contact us if you have any question:
info@belgianphysicalsociety.be).

Through your BPS membership, you will receive the *Belgian Journal of Physics*, with recent news from the world of physics in Belgium, didactic articles and announcements of conferences and seminars. You will have access to our new website (www.belgianphysicalsociety.be), where you can download past issues of the electronic magazine BPHY. You will also receive the 3 monthly magazine *Europhysics News* with latest news on physics and you can benefit from a 20% discount on all Springer books.

www.belgianphysicalsociety.be